The impact of SST biases in the tropical east Pacific and Agulhas current region on atmospheric stationary waves in the Southern Hemisphere

Chaim I. Garfinkel*

The Fredy and Nadine Herrmann Institute of Earth Sciences, The Hebrew University of Jerusalem, Edmond J. Safra Campus, Givat Ram, Jerusalem, Israel

Ian White

The Fredy and Nadine Herrmann Institute of Earth Sciences, The Hebrew University of Jerusalem, Edmond J. Safra Campus, Givat Ram, Jerusalem, Israel

Edwin P. Gerber

Courant Institute of Mathematical Sciences, New York University, New York, USA

Martin Jucker

Climate Change Research Center and ARC Centre of Excellence for Climate Extremes, University of New South Wales, Sydney, Australia

**Corresponding author address:* Chaim I. Garfinkel, The Fredy and Nadine Herrmann Institute of Earth Sciences, The Hebrew University of Jerusalem, Edmond J. Safra Campus, Givat Ram, Jerusalem, Israel.

E-mail: chaim.garfinkel@mail.huji.ac.il

ABSTRACT

Climate models in the Coupled Model Intercomparison Project, Phase 5 (CMIP5) vary significantly in their ability to simulate the phase and amplitude of atmospheric stationary waves in the midlatitude Southern Hemisphere. These models also suffer from a double inter-tropical convergence zone (ITCZ), with excessive precipitation in the tropical eastern South Pacific, and many also suffer from a biased simulation of the dynamics of the Agulhas Current around the tip of South Africa. The intermodel spread in the magnitude of the strength and phasing of SH midlatitude stationary waves in the CMIP archive is shown to be significantly correlated with the double ITCZ bias and biases in the Agulhas Return Current. An idealized General Circulation Model (GCM) is used to demonstrate the causality of these links by prescribing an oceanic heat flux out of the tropical East Pacific and near the Agulhas Current. A warm bias in tropical east Pacific SSTs associated with an erroneous ”double” ITCZ leads to a biased representation of midlatitude stationary waves in the austral hemisphere, capturing the response evident in CMIP models. Similarly, an overly diffuse sea surface temperature gradient associated with a weak Agulhas Return Current leads to an equatorward shift of the Southern Hemisphere jet by more than 3° and weak stationary wave activity in the austral hemisphere. Hence, rectification of the double ITCZ bias and a better representation of the Agulhas Current should be expected to lead to an improved model representation of the austral hemisphere.

1. Introduction

Policy makers and stakeholders need realistic projections of anthropogenic climate change in order to justify mitigation efforts and plan adaptation measures. The main tool for producing such projections are coupled ocean—atmosphere models used in climate assessments, such as the Coupled Model Intercomparison Project (CMIP). However, these projections differ among models even when identical forcings are applied, with across-model differences particularly pronounced on regional scales (Knutti and Sedláček 2013; He and Soden 2016; Garfinkel et al. 2020a), despite substantial model development and improvement in computational capacity.

The past few generations of CMIP models suffer from large biases in their climatology. There is evidence that these biases lead to spread and uncertainty in future projections. Specifically, many aspects of the changes in regional climate depend upon the unperturbed climatology (e.g. Held and Soden 2006; Matsueda and Palmer 2011; Scheff and Frierson 2012), and hence climatological biases could lead to unrealistic projections of anthropogenic climate change (Matsueda and Palmer 2011; He and Soden 2016). This limits the utility of projections of regional climate change from CMIP models.

The climate of the Earth is decidedly not zonally symmetric, even in the Southern Hemisphere. These zonal asymmetries, or stationary waves, are forced by asymmetries in the lower boundary, such as orography and the land-ocean distribution. Stationary waves control, in large part, the zonal structure of storm tracks (e.g., Inatsu and Hoskins 2004), which are closely linked to extreme wind and precipitation events (Shaw et al. 2016). Subtle shifts in stationary waves, such as those projected to occur under climate change (Wang et al. 2013; Simpson et al. 2014), can lead to profound impacts on regional climate.

The Southern Hemisphere stationary wave pattern is dominated by a zonal wavenumber 1 at both tropospheric and stratospheric levels (James 1988; Quintanar and Mechoso 1995a) with a ridge in the Pacific Ocean sector and a trough south of Africa and in the Indian Ocean sector (Figure 2a). The amplitude of this wave is largest at about 60S and is most pronounced during September and October in the upper troposphere and stratosphere (Quintanar and Mechoso 1995a). This stationary wave pattern is driven in part by Antarctic orography (James 1988), but with a more important contribution from a wavetrain propagating out of the tropical Indian Ocean with a ridge in the subtropical South Indian Ocean, a trough in the Indian sector of the Southern Ocean, and a ridge south of New Zealand (Quintanar and Mechoso 1995a,b, Figure 2a). This wavetrain is associated with the large-scale convective maxima that extends from the tropical northwestern Pacific to India (Inatsu and Hoskins 2004). Stronger convection in this region on interannual timescales is associated with a stronger stationary wave pattern (Peña-Ortiz et al. 2019). Southern Hemisphere stationary waves are also sensitive to frictional drag, with stronger drag leading to a stronger wave-1 pattern via transient eddies (Garfinkel et al. 2013a). Comprehensive climate models simulate a wide range of amplitudes and phases of this stationary wave pattern (figures 4.5 – 4.7 of CCM 2010), with some models simulating stationary waves twice as strong as observed and others with a phase difference of nearly 180° relative to those observed.

In this study we employ an idealized atmospheric general circulation model to explore the factors leading to biases in the midlatitude Southern Hemisphere stationary wave pattern. We focus on three systematic biases evident in many CMIP models.

1. Several generations of coupled climate models have suffered from the presence of a double inter-tropical convergence zone (ITCZ) in the South Pacific throughout the year (Mechoso et al. 1995; Lin 2007; Li and Xie 2014; Adam et al. 2016, 2018). In reality, an ITCZ does not

occur in the South Pacific except in March and April (Hubert et al. 1969; Zhang 2001). The severity of the double ITCZ bias in coupled model integrations is tightly linked to biases in the atmosphere component of that same model when fed with fixed sea surface temperatures (Xiang et al. 2017). The severity of this bias has been related to a range of processes in atmospheric models, including cloud radiative effects in the SH midlatitudes by some studies (Li and Xie 2014; Hwang and Frierson 2013) though not all (Kay et al. 2016; Adam et al. 2018), the convection scheme (e.g. Zhang and Wang 2006), and the formulation of the surface wind stress (e.g. Luo et al. 2005). A poorly simulated ITCZ (and associated Pacific cold tongue) in the mean state limit the confidence that can be placed in future projections of, e.g., El Nino-Southern Oscillation (ENSO) and its teleconnections (AchutaRao and Sperber 2006; Bellenger et al. 2014; Li et al. 2016; Bayr et al. 2019, among others) if the projected changes depend on the mean state (He and Soden 2016).

2. The Agulhas Current forms in the Mozambique Channel and transports heat poleward off the South African coast (Lutjeharms 2007). Beyond the southern tip of the Agulhas Bank off the southern coast of South Africa, the Agulhas Current retroflects, with most of its waters feeding the south Indian subtropical gyre in the Agulhas Return Current. About 10-20% of the current leaks westward into the adjacent South Atlantic (referred to as Agulhas Leakage), largely via rings and eddies with a characteristic spatial scale of around 100km (Lutjeharms 2007). The Agulhas Return Current extends from the Agulhas Retroflection ($\sim$20E) as far as 75E, and its passage east remains largely zonal. Climate models with a coarsely resolved ocean (i.e., most models participating in CMIP) struggle to capture the ocean dynamics behind the retroflection and leakage (Kwon et al. 2010; Holton et al. 2017). For example, models simulate too much leakage compared to observations by up to a factor of three, and

a concomitant reduction in retroflection, even if the strength of the Agulhas Current itself is accurately simulated (Weijer et al. 2012). The sharp gradient in surface temperature between the Agulhas Return Current and colder waters further poleward has been shown to influence local storm track activity in the lower troposphere (Inatsu and Hoskins 2004; Liu et al. 2007; Small et al. 2014; Yao et al. 2016), though the impacts on the broader scale circulation are less clear. Sampe et al. (2010) find that when a zonally symmetric SST gradient of similar strength to that near the Agulhas Return Current is inserted in a zonally symmetric aquaplanet model, the jet shift polewards, a result we return to in Section 5 of this study.

3. Most current climate models suffer from an equatorward bias in the position of the SH midlatitude jet as compared to observations (Wilcox et al. 2012; Swart and Fyfe 2012a; Bracegirdle et al. 2013) including some models with jet position 10 degrees from that observed, though this bias is reduced in the more recent Chemistry Climate Model Initiative models (Son et al. 2018). The magnitude of the simulated surface response to greenhouse gases and the ozone hole may depend on the severity of this bias, with models that exhibit a more equatorward climatological jet bias also showing a larger poleward shift of the jet in response to ozone depletion or greenhouse gases (Kidston and Gerber 2010; Garfinkel et al. 2013b; Sigmond and Fyfe 2014, among others), though such a relationship does not appear to be evident in the CCMI simulations (Son et al. 2018), nor in the ozone-only forced simulations presented by Seviour et al. (2017). Such a bias is also associated with incorrect surface wind stress on the Southern Ocean, and hence with a biased Southern Ocean circulation (Swart and Fyfe 2012a,b). Some studies have suggested that such a bias is in part due to biases in cloud distribution (Ceppi et al. 2012), though the full range of causes is still unclear.

This study aims to link these various biases together. In Section 2 we demonstrate that poorly simulated SH stationary waves are related to a double ITCZ and a too-weak surface temperature gradient near the Agulhas in CMIP models. In order to better establish the causality of this relationship, we have developed an idealized GCM of relevance to the SH atmospheric circulation, and we introduce this model and discuss key sensitivities in Section 3. We use integrations of this GCM to show that a double ITCZ is associated with a wavetrain pattern that degrades SH stationary waves (Section 4). Finally, we use this same idealized GCM to show that a poorly represented Agulhas return current leads to an overly equatorward jet latitude and too-weak stationary waves (Section 5).

2. Factors influencing the simulation of SH extratropical stationary waves in the CMIP5

We begin by considering the relationship between SH extratropical stationary waves and other biases in comprehensive climate models. We focus on 45 models that participated in the fifth phase of the Coupled Model Intercomparison Project (CMIP5) (Taylor et al. 2012) listed in Table 1.

a. Association between biased SH stationary waves and a double ITCZ

The observed precipitation climatology from 1979 through 2016 from the Global Precipitation Climatology Project (GPCP) version 2.3 (Adler et al. 2003) is in Figure 1a, and the corresponding multi-model mean precipitation over the period 1985 to 2004 in the historical period is shown in Figure 1b. The multi-model mean is characterized by too much precipitation in the tropical South Pacific (see the boxed region) as compared to that observed, and precipitation is larger than observed in all but two of the MIROC models (MIROC−ESM and MIROC−ESM−CHEM).

While this bias appears in nearly all models, its severity varies considerably. Figure 1c shows the precipitation climatology in models whose precipitation in the boxed region is between 100% and

175% of that observed, while Figure 1d shows the precipitation climatology in models whose precipitation in the boxed region is more than 250% of that observed. By construction, precipitation is larger in the tropical South Pacific in Figure 1d than in Figure 1c (Figure 1e).

The corresponding stationary waves, defined here as the deviation of the time-averaged geopotential height at 300hPa from its zonal average, is shown in Figure 2. The observed stationary wave pattern from ERA-5 is shown in Figure 2a. While the amplitude of the stationary waves are reasonable in the multi-model mean (Figure 2b), the phasing suffers from a bias: the maximum ridge is too far to the east (too close to South America and too far from New Zealand), and the trough is too concentrated in the South Indian Ocean and too weak south of Africa. These biases are more pronounced in models with a double ITCZ (Figure 2d) as compared to those with a single ITCZ (Figure 2c). The difference is characterized by a wave-3 pattern in midlatitudes (Figure 2e) with a deeper ridge over Australia in models with a double ITCZ and a trough in the midlatitude East Pacific, and this wavetrain may be associated with changes in the zonal distribution of rainfall in the tropical South Pacific.

The apparent relationship between the double ITCZ and biased stationary waves is summarized in Figure 3. For each model, the climatological precipitation in the boxed region on Figure 1 is compared to the difference in geopotential height between the red box and blue box on Figure 2, with the red box representative of the wave-1 ridge and the blue box representative of the wave-1 trough. The models included in Figure 1c and Figure 2c (less pronounced double-ITCZ models) are shown in red, while the models included in Figure 1d and Figure 2d (severe double-ITCZ models) are shown in green. The MIROC models are shown with a black x, and observations (GPCP precipitation and ERA5 heights) are shown with a grey diamond. The relationship between the double ITCZ and stationary waves is significant at the 5% confidence level using a two-tailed Student's-t test: models with a better simulated precipitation climatology in the SH tropics simulate more realistic stationary waves, and more than 35% of the variance in stationary waves is accounted for by the double ITCZ. The MIROC models are an exception to this general relationship, and these models are addressed in the discussion. The correlation is robust to variations of the spatial range of the red and blue boxes of $\sim 20\%$ (not shown). A similar correspondence is evident both in the annual mean and in June through November.

b. Relationship between biased SH stationary waves in CMIP5 and a weak Agulhas Return Current

The realism of SH stationary waves in CMIP5 models is also related to the quality of the representation of the Agulhas Current, and specifically, the tight meridional surface temperature gradient associated with the Agulhas Return Current. Figure 4a shows the meridional surface temperature gradient in ERA-5 data in the annual average, and Figure 4b is as in 4a but for the 45 CMIP5 listed in Table 1. While the multimodel mean represents the sharp gradient reasonably well, there is a wide diversity among the models. The models with a meridional temperature gradient in the Agulhas Return Current region (the black-boxed region) at least as strong as that observed are composited, and the mean surface temperature gradient for these models is shown in Figure 4c. The surface temperature gradient for a corresponding composite of models with a surface temperature gradient in this region less than 90% of the observed value is shown in Figure 4d. By construction, the models included in Figure 4d struggle to capture a strong gradient in this region. [1]

The corresponding stationary wave field in 300hPa geopotential height is shown in Figure 5, with the top two rows repeated from Figure 2. The stationary waves are stronger in those models

[1]Note that there is no relationship between the magnitude of the biased double ITCZ and the magnitude of the meridional surface temperature gradient near the Agulhas Return Current: the correlation of these in these 45 models is 0.04.

with a realistic surface temperature gradient near the Agulhas, as compared to models without such a gradient. This relationship is summarized in Figure 6. For each model, the climatological meridional surface temperature gradient in the boxed region on Figure 4 is compared to the difference in geopotential height between the red box and blue box on Figure 5, with the red box representative of the wave-1 ridge and the blue box representative of the wave-1 trough. The models included in Figure 4c and Figure 5c (stronger meridional gradient models) are shown in red, while the models included in Figure 4d and Figure 5d (overly diffuse Agulhas) are shown in green. The relationship between the strength of the surface temperature gradient and the amplitude of the stationary waves is significant at the 5% confidence level using a two-tailed Student's-t test: models with a better simulated surface midlatitude temperature gradient in the Agulhas Return Current region simulate more realistic stationary waves. The correlation is robust to variations of the spatial range of the red and blue boxes of $\sim 20\%$ (not shown). A similar correspondence is evident both in the annual mean and in June through November.

3. Towards a reasonable Southern Hemisphere circulation in an idealized model

While the results in Section 2 indicate a strong relationship between biased stationary waves and both a double ITCZ and a too-weak meridional SST gradient associated with the Agulhas Return Current, the causality of this connection is unclear. For example, Figure 1c and Figure 1d differ not just in the tropical South Pacific, and Figure 4c and Figure 4d differ not just near South Africa, hence it is unclear how much of the stationary wave response is associated with the altered precipitation pattern in the tropical South Pacific and surface temperature pattern south of Africa. In order to investigate the causality of this relationship, we have developed a simplified general circulation model that represents the Southern Hemisphere stationary waves and jet in order to understand their connections to SST biases in comprehensive climate models.

We begin with the model of an idealized moist atmosphere (MiMA) introduced by Jucker and Gerber (2017) and Garfinkel et al. (2020b). This model builds on the aquaplanet model of Frierson et al. (2006), Frierson et al. (2007), and Merlis et al. (2013). Very briefly, the model solves the moist primitive equations on the sphere, employing a simplified Betts-Miller convection scheme (Betts 1986; Betts and Miller 1986), idealized boundary layer scheme based on Monin-Obukhov similarity theory, a slab ocean, the Rapid Radiative Transfer Model (RRTMG) radiation scheme (Mlawer et al. 1997; Iacono et al. 2000), and gravity waves following Alexander and Dunkerton (1999) and Cohen et al. (2013). Please see Jucker and Gerber (2017) for more details. Unless otherwise indicated, all simulations in this paper were run with a triangular truncation at wavenumber 42 (T42; equivalent to a roughly 2.8° grid) with 40 vertical levels for 48 years, with the first 10 years treated as spinup.

Following Garfinkel et al. (2020b), we have added three sources of zonal asymmetry to the lower boundary of an initially zonally symmetric moist aquaplanet model: orography, ocean horizontal heat fluxes, and land-sea contrast (i.e., difference in heat capacity, surface friction, and moisture availability between oceans and continents). The specification of these forcings (especially the ocean horizontal heat fluxes) has been updated from Garfinkel et al. (2020b), and the updated analytic formulae are included in the appendix. The total ocean horizontal heat update is shown in Figure 7a, and the atmospheric surface temperatures in ERA-5 reanalysis and in the model are shown in figure 7b and figure 7c respectively. We assess sensitivity to the representation of the Andes, which are smeared out at T42 resolution, below. This default model configuration is referred to as CONTROL in the rest of this paper.

The resulting stationary waves in CONTROL are shown in Figure 8a. The SH stationary waves represent observed stationary waves as realistically as the multi-model mean of the CMIP5 and certainly better than the group of models with a double ITCZ (Figure 2d), though the entire pattern is shifted equatorward by $\sim 5^{\circ}$ as compared to observations (Figure 2a). The latitude of maximum winds at 820hPa (i.e. jet latitude) in the control integration is 50.4°S in the annual average, which is better than that in most CMIP models (Wilcox et al. 2012; Swart and Fyfe 2012a; Bracegirdle et al. 2013): the average jet latitude in the 45 models considered here is 49.2°S.

We find that the Northern Hemisphere stationary wave pattern is degraded under the configuration of ocean heat fluxes used here, when compared to the configuration of Garfinkel et al. (2020b), when both are run at T42 resolution (not shown). However an increase in resolution from T42 to T85 in the configuration used here leads to improved stationary waves in the Northern Hemisphere. Previous work has found that high resolution is needed in order to capture the full response to a narrow Gulf and Kuroshio (Minobe et al. 2008; Xu et al. 2011; Small et al. 2014; Yao et al. 2016). The configuration of Garfinkel et al. (2020b) imposed broad regions of warming associated with the Gulf and Kuroshio, and hence we suspect that the atmosphere could respond in a more realistic manner even at T42. In the rest of this paper we focus on the SH only.

The importance of ocean horizontal heat fluxes for SH stationary waves is demonstrated in Figure 8b, which shows the stationary waves that result if we include land-sea contrast and orography as in the control simulation, but without any zonally asymmetric ocean heat flux (we still apply a zonally uniform meridional ocean heat flux, equation 4 in the appendix). The SH stationary waves are significantly weaker, and the degradation of the ridge near New Zealand is particularly acute. Hence, the comparison of Figure 8a and Figure 8b illustrates how crucial zonal ocean heat fluxes are to the SH climatology.

The degradation in SH stationary waves when east-west ocean heat fluxes are excluded in Figure 8b is associated with overly zonal precipitation in the deep Tropics. Figure 9 shows the climatology of precipitation in CONTROL and in the simulation in which east-west ocean heat fluxes are excluded. While the simulation of the land precipitation is qualitatively similar (including the

Indian monsoon, not shown) compared to that in the control simulation when east-west ocean heat fluxes are excluded (bottom of Figure 9), precipitation in the deep tropics is not enhanced in the far West Pacific relative to the east, and Indian Ocean precipitation is also too-zonal. This result suggests that midlatitude SH stationary waves are very sensitive to the zonal structure of precipitation in the tropics.

The stationary waves when the model is run at double the resolution (T85 truncation) are shown in Figure 8c. The stationary waves are similar at T42 and T85, though there are two notable differences: the stationary waves are somewhat weaker and shifted poleward at T85. The latitude of the lower tropospheric zonal wind maximum (i.e., the extratropical jet) is also shifted poleward by $\sim 0.6^{\circ}$ at T85. The higher resolution integration better captures the sharp transition from a ridge to a trough downstream of South America (Figure 8a vs Figure 8c), possibly due to its ability to better resolve the Andes. In summary, the structure of the stationary waves is improved at T85, though the amplitude is not. Given the overall similarity of the T42 and T85 integrations, we focus on lower resolutions integrations for the remainder of the study.

Observed topography is used for the most realistic experiment, albeit at the resolution of the model with no effort to adjust the amplitude to preserve ridge heights (sometimes referred to as envelope topography), but with regularization as in Lindberg and Broccoli (1996). We set the "ocean topog smoothing" parameter of this scheme to 0.995 to minimize Gibbs ripples over the Himalayas and Andes. T42 resolution smears out the Andes, and it is conceivable that this would degrade the stationary waves. Figure 8d assesses sensitivity to the effective ridge height of the Andes. Before the regularization procedure is performed, we first multiply the observed topography in the region 6S-63S, 230E-300E by a factor of 1.75. The net effect is that after topography regularization is completed the maximum ridge heights are similar to the maximum gridscale ridge heights from observations; this modification is often referred to as enforcing envelope topography.

The stationary waves in Figure 8a and in Figure 8d are nearly indistinguishable however. Thus the representation of the Andes has little effect on the large scale stationary waves. This lack of sensitivity appears to be consistent with that found by Takahashi and Battisti (2007) (see their figure 6), who find that the remote effect of the Andes saturates for realistic topographic heights.

4. Impact of a double ITCZ

We now use the idealized model introduced in Section 3 to understand the impact of biases in tropical SSTs and precipitation (i.e., a double ITCZ) on extratropical stationary waves. Figure 7 shows the surface temperatures in CONTROL and observed, and while the idealized model represents the large scale pattern of surface temperatures, biases are present in e.g. the tropical South Pacific. Our approach is to add heat fluxes to the ocean to reduce (or accentuate) SST biases, and hence improve (or degrade) tropical precipitation. We can then understand how the extratropical atmosphere responds to these changes in the tropics. To do this, we will consider two different perturbations, one focused on meridional heat transport, the second zonal heat transport. These two strategies allow us to assess the robustness of our approach.

We first "impose" a double ITCZ by modifying the meridional heat fluxes of the slab ocean in the tropical Southern Hemisphere (Figure 10a), comparing to an analogous simulation in which the ocean heat flux perturbation is of opposite sign (Figure 10b), in order to improve the signal to noise ratio. The functional form for the perturbation is included in the appendix. In both cases no net heating is added. Rather, the ocean heat flux in CONTROL is simply redistributed, ensuring similar globally averaged temperatures. When extra heat is fluxed out of the tropical South-East Pacific and into the extratropical Pacific (Figure 10b), the region of cold tropical SSTs and reduced precipitation is larger as compared to a simulation with less flux of heat out of the tropical South Pacific (Figure 10df vs. Figure 10ce). Associated with this imposition of a double

ITCZ is strengthened divergence at 300hPa in the tropical South-East Pacific (boxed region on Figure 10g as compared to Figure 10h), coupled with reduced divergence over the South Pacific Convergence Zone (SPCZ) region further west. This dipole in divergence weakens the Rossby wave source dipole (computed as in Sardeshmukh and Hoskins 1988, using daily data) in the tropical South Pacific in the double ITCZ integration (Figure 10i), compared to the integration with a single ITCZ (Figure 10j).

The net effect on stationary waves is shown in Figure 11. SH stationary waves are stronger in the simulation with a single ITCZ (Figure 11b), and more closely resemble those observed (Figure 11e). The difference in the stationary waves between the two simulations is shown in the right column of Figure 11, and the stationary wave pattern is weakened south of Africa and near New Zealand in response to a double ITCZ. In addition to the subpolar changes, there is a deeper trough near 120W in the subtropics for a single ITCZ, which is related directly to the lack of subtropical precipitation further equatorward and changes in the Rossby wave source. This change in the trough near 120W in the subtropics initiates a poleward propagating Rossby wave train that appears to encompass most of the extratropics (right column of Figure 11). This difference in the stationary waves between the two simulations can be compared to the difference in stationary waves between CMIP5 models with a severe ITCZ bias and a moderate ITCZ bias (Figure 2d). An enhanced ridge near New Zealand and trough south of Africa are common to both.

We next assess the sensitivity of the stationary waves to the pattern of the SSTs, by alternately "imposing" a double ITCZ in a second experiment in which heat fluxed out of the tropical East Pacific is redistributed to the tropical West Pacific. We again compare to a parallel integration in which the ocean heat flux perturbation is imposed with the same pattern but opposite sign. The difference in ocean heat uptake for the pair of integrations (double-single) is shown in Figure 12a:

there is a strong zonal dipole in heat uptake in the Pacific, which either eliminates the climatological zonal dipole or accentuates it. As before no net heating is added.

A zonal dipole in ocean heat uptake leads to a similar dipole in surface temperature distribution (Figure 12b), and also to a similarly structed precipitation anomaly with either a South Pacific convergence zone or a double ITCZ (Figure 12c). Changes in tropical divergence in the tropical South Pacific (Figure 12d) resemble those in Figure 10gh: a zonally oriented dipole is stronger for the single ITCZ cases in Figure 12d than for the double ITCZ case. Consistent with this, the zonal dipole in Rossby wave source in the South Pacific is stronger for a single ITCZ (Figure 12e).

This difference in tropical precipitation affects SH stationary waves (Figure 11cd). The amplitude of the the SH stationary waves increases when the double ITCZ bias is eliminated, leading to a closer correspondence with observations (Figure 11e). The difference in the stationary waves between the two simulations can be compared to the difference for a meridonal dipole and for CMIP data (Figure 2d). While the details of the responses to a meridional and zonal dipole differ, an enhanced trough in the subpolar Pacific near 120W and ridge south of Africa are evident in both, as is the deeper trough near 120W in the subtropics for a single ITCZ. This commonality suggests that the biased-phase of stationary waves in CMIP5 models with a double ITCZ (Figure 2d) is caused by biases in the tropical East Pacific. Spurious precipitation in the tropical East Pacific leads to a spurious local Rossby wave source, which generates a wavetrain into the South Pacific that is out of phase with the climatological stationary wave pattern leading to destructive interference and a weak amplitude and incorrect phase.

The changes in stationary waves assocaited with the ITCZ also affects the stratosphere. Namely, the double ITCZ change is associated with a stronger stratospheric polar vortex ($\sim$ 6m/s increase in zonal winds at 10hPa, 55S) as compared to the simulations with a single ITCZ. More comprehensive models suffer from a too-strong vortex. This work suggests the importance of tropical precipitation for the entire stratosphere-troposphere system.

5. Impact of an overly diffuse Agulhas current

We now consider the connection between SST biases in the Agulhas region, and specifically a weakened meridional temperature gradient off the coast of Africa associated with a diffuse Agulhas Return Current, and biases in the simulation of the extratropical jet and stationary waves in the SH. We modify the SSTs in the Agulhas region as show in Figure 13ab. In Figure 13a, the zonally localized SST gradient associated with the Agulhas is enhanced as compared to CONTROL, while in Figure 13b the zonally localized SST gradient is removed. As before, no net heating is added, rather the ocean heat flux in CONTROL is redistributed to approximate the impact of Agulhas current retroflection. The functional form of the ocean heat flux perturbation is given in equation 7. By construction, the surface temperature meridional gradient is stronger in Figure 13c as compared to Figure 13d.

A sharper surface temperature meridional gradient near the Agulhas leads to changes in stationary waves. Figure 14a shows the stationary wave pattern in the simulation with enhanced regional structure, while Figure 14b shows the stationary wave pattern when regional structure associated with the Agulhas is removed. The stationary wave pattern is both stronger and located further poleward in Figure 14a, and is more realistic than that shown in Figure 14b except in the Atlantic sector where there is too strong of a ridge as compared to ERA-5 (Figure 14e). The pattern of changes in the stationary waves broadly resembles that seen in CMIP models in Figure 5e, indicating that the relationship seen in CMIP5 models is indeed forced by the surface temperature gradient.

How does an enhanced surface temperature gradient in the Agulhas Return Current region lead to stronger stationary waves? We first consider and reject three hypotheses - Rossby wave source, changes in eddy activity, and changes in jet latitude - before focusing on the importance of the zonal structure of the upper level temperature response to a zonally localized Agulhas perturbation. We begin with changes in precipitation in Figure 13ef. Local changes in precipitation appear as expected, with enhanced precipition over the region that warms and supressed precipitation over the region that cools, in addition to precipitation changes elsewhere. Changes in the Rossby wave source resemble a dipole mimicing the precipitation dipole evident as in Figure 13ef (not shown), and do not seem to be capable of explaining the behavior seen.

Eddy activity increases in response to the increase in the local meridional temerpature gradient. Figure 13gh shows the transient kinetic energy in the lower troposphere, $\frac{u'^2+v'^2}{2}$, where u' and v' are the high pass filtered zonal and meridional winds obtained by applying a 5th order Butterworth filter with an 8-day cutoff. Consistent with Sampe et al. (2010), transient kinetic energy is increased in the presence of a stronger surface temperature gradient. A similar increase in transient kinetic energy aloft, and in eddy zonal-momentum ($u'v'$) and heat ($v'T'$) flux by the meridional wind, also occurs in response to a tighter SST gradient (not shown; consistent with the energetic arguments of Mbengue and Schneider (2017)).

While it is tempting to naively conclude that enhanced eddy activity necessarily leads to stronger stationary waves, such an assumption is, in fact, incorrect. It is helpful to contrast the changes in stationary waves in response to an enhanced surface temperature gradient in the Agulhas Return Current region to changes in stationary waves when a zonally symmetric ocean heat flux perturation at these same latitudes is applied. Figure 15a is similar to Figure 13ab, but the ocean heat flux perturbation is applied in a zonally symmetric manner (see equation 8). This leads to surface temperature and precipitation perturbations that mimic those in Figure 13cdef in the Agulhas region, except that they are zonally symmetric. It is clear from Figure 15d that transient kinetic energy also increases, and in both Figure 13gh and Figure 15d the strengthening of eddy activity extends over much of the extratropics. However, changes in stationary waves are weak for the zonally symmetric perturbation (Figure 14cd) and do not resemble those for a zonally confined perturbation (Figure 14ab) or in CMIP5 data. Hence, a zonally symmetric change does not yield the same stationary wave response even if eddy activity increases, i.e. the confinement to the Agulhas region is particularly important.

The latitude of the jet maximum increases in response to a stronger surface meridional temperature gradient in the Agulhas return current region. Specifically, the surface jet is shifted more than 3° poleward if the regional structure of the Agulhas is included (Figure 13ij). Note, however, that there is no statistically significant relationship between jet latitude and the strength of the surface temperature meridional gradient in this region in CMIP5 models. Furthermore, the surface jet is shifted poleward by 4° if a zonally symmetric perturbation is included (Figure 15e), yet changes in stationary waves are weak in Figure 14cd and do not resemble those in Figure 14ab (except near South America, which we speculate may be due to changes in orographic generation of stationary waves from the Andes due to a change in jet latitude). Hence the stationary wave response to SSTs in the Agulhas return current region is not directly associated with the jet shift caused by these anomalous SSTs.

Thus far we have shown that the stationary wave response is not associated with the Rossby wave source, jet latitude, or changes in eddy activity. In contrast, the stationary wave response can be understood (in a diagnostic sense) using the thermodynamic budget of Wills and Schneider (2018) and Garfinkel et al. (2020b). The thermodynamic budget relies on changes in temperature aloft, and hence we show changes in 300hPa temperature in Figure 13kl and Figure 15f for a zonally confined and zonally symmetric pertubation respectively, A local ocean heat flux perturbation near the Agulhas leads to local changes in upper level temperature (Figure 13kl), while a zonally symmetric ocean heat flux perturbation leads to a zonally symmetric response of upper level temperature (Figure 15f). In both, in the same region in which transient eddy kinetic activity is increased, temperatures aloft also increase; that is, the the stronger eddy activity in response to a stronger meridional surface temperature gradient leads to a warming of the midlatitudes while slightly cooling subtropical latitudes. While the increase in transient kinetic energy is present both for the zonally symmetric perturbation and also when the perturbation is confined to near the Agulhas, the increase in Figure 15gh is zonally symmetric and does not extend towards Africa.

This zonal structure of the upper level temperature allows for a diagnostic interpretation of the stronger stationary waves in Figure 14ab as compared to Figure 14cd. Namely, only for a zonally confined perturbation does the Agulhas perturbation modify zonal advection of temperature, and hence to a change in meridional advection of temperature in order to maintain a steady state budget. A change in the meridional advection of temperature mandates a change in the meridional wind, and hence an altered stationary wave pattern (not shown).

Overall, only a localized change in the Agulhas region gives similar stationary wave changes to that seen in CMIP5. A zonally symmetric change does not yield the same stationary wave response, i.e. the Agulhas region is crucial.

6. Discussion and Conclusions

Climate change projections differ among models, with across-model differences particularly pronounced at regional scales (Knutti and Sedláček 2013; He and Soden 2016; Garfinkel et al. 2020a). While some of this spread is likely due to internal variability in the climate system, and hence is irreducible, much of the spread may arise from model biases. Reducing these biases would allow us to reduce the uncertainty in future circulation trends. There is substantial evidence that an improved basic state climatology will improve regional climate projections (e.g. Held and Soden 2006; Matsueda and Palmer 2011; Scheff and Frierson 2012; Ogawa et al. 2015; He and Soden 2016). Here we considered processes that impact Southern Hemisphere stationary waves, focusing on the role of two systematic biases that appear in many CMIP models: a spurious inter-tropical convergence zone (ITCZ) in the South Pacific, and a too-weak sea surface temperature gradient in the Agulhas at the tip of South Africa.

A double ITCZ was shown to bias stationary waves in the midlatitude Southern Hemisphere. Specifically, spurious precipitation in the tropical South Pacific is associated with anomalous upper tropospheric divergence and a Rossby wave source that weakens the climatological zonal dipole in the South Pacific. This spurious Rossby wave source generates a wavetrain into the South Pacific which is largely out of phase with the existing stationary wave pattern. Specifically, the stationary wave pattern in response to a spurious double ITCZ includes a ridge south of Africa and trough near New Zealand, both of which destructively interfere with the stationary waves otherwise present. This relationship is evident both in CMIP5 integrations and in targeted experiments of an idealized atmospheric model.

Two versions of one CMIP5 model, MIROC−ESM and MIROC−ESM−CHEM, provide an exception to this relationship. They exhibit a single ITCZ, yet poorly represent SH stationary waves (see the black dots in Figure 3). While these models exhibit a better climatological precipitation than any other CMIP5 model in the South Pacific, they suffer from too-much precipitation in the Indian Ocean and an overly weak South Pacific Convergence Zone (figure 6cd of Watanabe et al. 2011). The net effect is that tropical precipitation is overly zonal. The high biased precipitation in the Indian Ocean in particular is an outlier as compared to the other models we have examined, and exceeds observed precipitation by a factor of two. As is evident in Figure 8b and 9b, an overly zonal climatology of tropical precipitation leads to biased stationary waves. Hence the overly weak stationary waves in this model can be associated with an overly zonal precipitation structure, despite its relative success in the East and Central Pacific. Note that the high resolution MIROC4h model has a more realistic tropical precipitation climatology in the Indian Ocean than the lower resolution MIROC models, and consistent with this, has a reasonable stationary wave pattern.

In Section 5, we showed that an overly diffuse Agulhas Return Current leads not only to biases in local precipitation and temperature, but also to changes in eddy activity throughout much of the extratropical Southern Hemisphere. A sharper surface temperature gradient in the Agulhas Return Current region leads to enhanced eddy activity (Inatsu and Hoskins 2004; Small et al. 2014; Yao et al. 2016) and a warming of midlatitudes and a cooling of the subtropics. The net effect of these changes is a poleward shift in the Southern Hemisphere jet by more than $3°$ and stronger stationary waves.

The jet shift is generally consistent with those of Sampe et al. (2010), though they imposed a zonally symmetric SST gradient of similar strength to that near the Agulhas Return Current in a zonally symmetric aquaplanet model. While is it tempting to conclude that most CMIP5 models lack the resolution to resolve the key processes in the Agulhas (and consistent with this, the jet latitude is typically too far equatorward), there is no statistically significant relationship between jet latitude and the strength of the surface temperature gradient in the region of Agulhas Return Current in CMIP5 models.

There is, however, a statistically significant relationship between the strength of the surface temperature gradient in the region of Agulhas Return Current and the strength of SH stationary waves in CMIP5. Specifically models with a stronger surface temperature gradient simulate stronger SH stationary waves both in CMIP5 and in our idealized model. This strengthening of stationary waves cannot be explained by analyzing changes in the Rossby wave source, by an increase in eddy activity, or by the change in jet latitude. Rather, it appears to be associated with the localization of the perturbation to the Indian Ocean basin.

SH stationary waves are of curcial importance for the stratospheric vortex (Wirth 1991; Scott and Haynes 2002). Comprehensive models have long suffered from a cold pole problem in the stratosphere, which complicates ozone forecasts: a cold pole leads to more ozone loss. Our results suggest that longstanding biases in the representation of the troposphere (and associated biases in precipitation, particularly in the tropics) may play a key role in this bias. Indeed, the simplified model integrations with better SH stationary waves exhibit a weaker vortex and warmer polar cap temperatures.

Overall, we have shown that common model biases in the representation of the Southern Hemisphere in general circulation models are linked: an inter-tropical convergence zone (ITCZ) in the South Pacific leads to a worsening of stationary waves in the Southern Hemisphere, while an overly diffuse Agulhas is associated with too-weak stationary waves and an equatorward shift of the jet. Hence, progress towards removing the double ITCZ bias and a better representation of the Agulhas Current should be expected to lead to an improved model representation of the extratropical large-scale circulation.

7. Appendix: A model of an idealized moist atmosphere (MiMA) of relevance to the Southern Hemisphere

We now document the changes made to MiMA as compared to Garfinkel et al. (2020b). Code for this model configuration will be made available on GitHub as part of the MiMA v2.0 release.

a. Land-sea contrast

As in Garfinkel et al. (2020b), we add three different aspects of land-sea contrast: the difference in mechanical damping of near surface winds between the comparatively rough land surface vs. the smooth ocean, the difference in evaporation between land and ocean, and the difference in heat capacity. The roughness lengths for momentum over ocean and land, and also for moisture exchange over ocean, is identical to that in Garfinkel et al. (2020b) and not repeated here for brevity. The roughness lengths for moisture exchange over land in Garfinkel et al. (2020b) was $3.21 \cdot 10^{-17}$m independent of latitude, which led to too much evaporation in the subtropics and not enough evaporation in the deep tropics when compared to reanalysis. Here, we have added latitudinal dependence to the representation of the roughness lengths for moisture over land, or $z_{oh}\mathrm{land}$ as follows:

$$z_{oh}\mathrm{land} = 10^{-7}\exp\left(\frac{-|\phi|^3}{2*15^\circ}\right) + 10^{-25}\exp\left(\frac{-|\phi-45^\circ|^3}{2*30^\circ}\right) + 10^{-25}\exp\left(\frac{-|\phi+45^\circ|^3}{2*30^\circ}\right)\ \mathrm{meters} \tag{1}$$

where ϕ is latitude, which leads to increased evaporation near the equator. These parameters were selected via trial and error in order to generate reasonable evaporation for the most realistic experiment as compared to reanalysis data.

The heat capacity for land grid points is set to $1 \cdot 10^7\ JK^{-1}m^{-2}$ (equivalent to a mixed layer depth of 2.5m). For oceanic grid points the heat capacity is set to

$$Cocean = \begin{cases} 1 \cdot 10^8 \frac{J}{Km^2} & , \quad |\phi| < 20^\circ \\ 1 \cdot 10^8 \frac{J}{Km^2} \cdot (1. - \frac{|\phi|-20^\circ}{60^\circ-20^\circ}) + 3 \cdot 10^8 \frac{J}{Km^2} \frac{|\phi|-20^\circ}{60^\circ-20^\circ} & , \quad \text{otherwise} \\ 3 \cdot 10^8 \frac{J}{Km^2} & , \quad |\phi| > 60^\circ \end{cases} \tag{2}$$

which corresponds to a mixed layer depth that smoothly increases from 25m in the tropics to 75m in polar regions. This reduction in the tropical mixed layer depth leads to a more realistic surface temperature and precipitation seasonal cycle as compared to the higher values used in Garfinkel et al. (2020b), as documented in Jucker (2019). Note that this option was included in the original MiMA release (Jucker 2017). For experiments with no land-sea contrast the oceanic mixed layer depth and roughness is used everywhere. We use a high resolution land-mask to determine land versus ocean; thus, the surface is accurately represented on the latitude vs. longitude grid on which e.g. surface fluxes are computed.

For experiments with land-sea contrast, we set the albedo as

$$\text{albedo} = 0.23 + \frac{0.80-0.23}{2} \cdot \left[1 + \tanh\left(\frac{\phi - 68^\circ}{5^\circ}\right)\right] + \frac{0.80-0.23}{2} \cdot \left[1 - \tanh\left(\frac{\phi + 65^\circ}{5^\circ}\right)\right] \tag{3}$$

which leads to higher albedo values over the Arctic and Antarctic that smoothly transition to 0.23 in the midlatitudes and tropics, except for the following regions:

1. Australian desert: $118^\circ < \lambda < 145^\circ$ and $-30^\circ < \phi < -19^\circ$
2. Gobi desert: $80^\circ < \lambda < 100^\circ$ and $32^\circ < \phi < 37^\circ$; $80^\circ < \lambda < 110^\circ$ and $37^\circ \leq \phi < 41^\circ$; $80^\circ < \lambda < 115^\circ$ and $41^\circ \leq \phi < 49^\circ$
3. Saharan/Arabian desert: $345^\circ < \lambda$ or $\lambda < 50^\circ$, $13^\circ < \phi < 30^\circ$

where the albedo is set to 0.43. λ is longitude. The increased albedo over desert regions helps to ensure that the monsoon does not extend too far poleward into a region that is actually desert. A full discussion of the monsoons in MiMA is deferred to future work. MiMA has no clouds, and an albedo of 0.23 was primarily tuned to approximate the shortwave effects of clouds and lead to tropical surface temperature similar to those observed. For experiments with no land-sea contrast the albedo is set to 0.27 everywhere in order to maintain a similar tropical surface temperature.

b. East-west ocean heat fluxes

Garfinkel et al. (2020b) introduced ocean horizontal heat uptake (often referred to as Q-fluxes e.g. Merlis et al. 2013) that mimicked those observed on the large-scale. Here we specify Q-fluxes on a much more regional scale in order to capture sharp surface temperature gradients associated with e.g., the Agulhas Current. These Q-fluxes are necessary as we do not have a dynamical ocean. The net effect of these formulae is shown in figure 7, which compares favorably to the Q-fluxes inferred from an ocean reanalysis by Forget and Ferreira (2019) (see their figure 1) or from a top-down Earth system energy budget in Trenberth et al. (2019) (see their figure 2) or Trenberth and Fasullo (2018) (see their figure 7). The only region in which we systematically deviate from the ocean heat uptake of Forget and Ferreira (2019) is the tropical Pacific, where we have heat diverging away and converging in the high latitudes Southern Hemisphere. The experiments in the text with and without a double ITCZ can be thought of as sensitivity tests to including such an ocean heat flux.

We now present the analytical formulae used to specify ocean heat fluxes. All integrations include the zonally-uniform ocean horizontal heat uptake of Merlis et al. (2013), Jucker and Gerber (2017), and Garfinkel et al. (2020b), which is specified as

$$\nabla \cdot \mathbf{F}_o(\phi) = Q_o \frac{1}{cos\phi}\left(1 - \frac{2\phi^2}{\phi_o^2}\right) exp\left(-\frac{\phi^2}{\phi_o^2}\right) \quad (4)$$

with Q_o=26W/m^2 and $\phi_o = 16^\circ$ (repeated from equation 2 of Jucker and Gerber 2017; Merlis et al. 2013).

In addition, we prescribe several different components of the east-west ocean horizontal heat uptake. As described below, each individual component adds negligible net heating to the atmosphere. When all are summed together, no net heating is added to the atmosphere (the residual heatings add up to zero). Specifically, anomalies in globally averaged surface temperature over the duration of the 38 year CONTROL integration are less than 0.3K (i.e. the model is fully spun-up and does not drift). Many of the perturbations described below are of the form

$$\nabla \cdot \mathbf{F} = \sum A_n \cdot \exp(-\frac{(\lambda - \mu_{\lambda n})^2}{2 \cdot \sigma_{\lambda n}^2}) \cdot \exp(-\frac{(\phi - \mu_{\phi n})^2}{2 \cdot \sigma_{\phi n}^2}), \tag{5}$$

and for these perturbations we include tables of the parameters A_n, $\mu_{\lambda n}$, $\sigma_{\lambda n}$, $\mu_{\phi n}$, and $\sigma_{\phi n}$.

c. Agulhas Current

The representation of the Agulhas current, Agulhas Leakage, the Agulhas Return Current, cold upwelling off the coast of Namibia, and a cooler tropical West Indian Ocean in the region $2^\circ \leq \lambda \leq 100^\circ$ and $-60^\circ \leq \phi \leq 35^\circ$ is specified with the parameters in Table 2 applied to equation 5.

To ensure that there is little cooling over tropical Africa and weak cooling over the tropical West Indian Ocean, we specify

$$\nabla \cdot \mathbf{F}_{\text{Africa}} = \begin{cases} 25\frac{W}{m^2} \cdot (1 - (\frac{\phi}{35^\circ})^2) \cdot \cos(5(\lambda - 28^\circ)) & , \quad 10^\circ \leq \lambda \leq 82^\circ \text{ and } |\phi| < 35^\circ \\ 0 & , \quad \text{otherwise} \end{cases} \tag{6}$$

Finally, we add heat to the atmosphere near the African coast, by specifying

$$\nabla \cdot \mathbf{F}_{\text{Agulhas}} = \left\{ +(38 + \text{Africaextra}/3)\frac{W}{m^2} \cdot \exp(-\frac{(\lambda - \frac{2}{3}\phi - 57^\circ)^2}{2 \cdot 16}) \cdot \exp(-\frac{(\lambda + \phi - 10^\circ)^2}{2 \cdot 15^{\circ 2}}) \right. \quad , \tag{7}$$

in the region $2^\circ \leq \lambda \leq 100^\circ$ and $-60^\circ \leq \phi \leq 35^\circ$.

Africaextra is alternately set to $70\frac{W}{m^2}$ or $-70\frac{W}{m^2}$ in section 5. For the simulations with a zonally symmetric Agulhas perturbation, Sampeterm is alternately set to $25\frac{W}{m^2}$ or $-25\frac{W}{m^2}$ and the perturbation is specified as.

$$\nabla \cdot \mathbf{F}_{\text{Agulhas}} = \begin{cases} +\text{Sampeterm} \cdot 0.8822 \cdot \frac{W}{m^2} \cdot \exp(-\frac{(\phi+40^\circ)^2}{2 \cdot 4^{\circ 2}}) & , \\ -\text{Sampeterm}\frac{W}{m^2} \cdot \exp(-\frac{(\phi+48^\circ)^2}{2 \cdot 4^{\circ 2}}) & , \\ 0 & , \quad \text{otherwise} \end{cases} \tag{8}$$

d. Pacific sector

We begin with a representation of the Pacific warm pool similar to that in Garfinkel et al. (2020b)

$$\nabla \cdot \mathbf{F}_{\text{Pac}} = \begin{cases} (1-(\frac{\phi}{35^\circ})^4) \cdot Q_{\text{Pacific}} \cdot \cos(5/3(\lambda - 140^\circ)) & , \quad 86^\circ \leq \lambda \leq 302^\circ \text{ and } |\phi| < 35^\circ \\ 0 & , \quad \text{otherwise} \end{cases} \tag{9}$$

as a first step onto which we add smaller scale features in order to represent observed ocean heat fluxes, with $Q_{\text{Pacific}} = 18\frac{W}{m^2}$.

In order to better confine the cold tongue to oceanic regions, we include:

$$\nabla \cdot \mathbf{F}_{\text{CTpart1}} = \begin{cases} (1-(\frac{\phi}{35^\circ})^4) \cdot Q_{\text{Pacific}} \cdot \sin(8(\lambda - 279.5^\circ)) & , \quad 257^\circ \leq \lambda \leq 302^\circ \text{ and } |\phi| < 35^\circ \\ 0 & , \quad \text{otherwise} \end{cases} \tag{10}$$

The representation of the Cold Tongue is made more realistic by fluxing heat out of the equatorial East Pacific and towards the West Pacific and subpolar South Pacific. In the region $129^\circ \leq \lambda \leq 290^\circ$ and $-78^\circ \geq \phi \leq 24^\circ$, we specify the parameters in Table 3 applied to equation 5.

ITCZNS and ITCZEW are the parameters modified in Section 4. ITCZEW is alternately set to $30\frac{W}{m^2}$ or $-30\frac{W}{m^2}$, and ITCZNS is alternately set to $25\frac{W}{m^2}$ or $-25\frac{W}{m^2}$.

In order to avoid strong oceanic heat uptake over regions that are actually continents, we modify the heat flux near Australia. Over the region $50^\circ \leq \lambda \leq 220^\circ$ and $-36^\circ \leq \phi \leq 10^\circ$, we specify the parameters in Table 4 applied to equation 5. The net effect of this is to prevent a flux of heat into the atmosphere over subtropical Australia that would otherwise be imposed in Equation 9. This extra heat flux into the atmosphere instead occurs over the Indian Ocean, and thus represents Indonesian Throughflow.

In order to represent the Kuroshio current, we add in the region $110^\circ \leq \lambda \leq 270^\circ$ and $5^\circ \geq \phi \leq 47^\circ$

$$\nabla \cdot \mathbf{F}_{\text{Kuroshio}} = \begin{cases} Q_{\text{Kuroshio}} \cdot \exp(-\frac{(\lambda - 3\phi - 45^\circ)^2}{2 \cdot 100}) \cdot \exp(-\frac{(\lambda + \phi - 170^\circ)^2}{2 \cdot 20^{\circ 2}}) & , \\ -Q_{\text{Kuroshio}} \cdot 0.594 \cdot \exp(-\frac{(\lambda + \phi - 268^\circ)^2}{2 \cdot 49}) \cdot \exp(-\frac{(\lambda - \phi - 215^\circ)^2}{2 \cdot 625}) & , \\ 0 & , \quad \text{otherwise} \end{cases} \tag{11}$$

where $Q_{\text{Kuroshio}} = 40 \frac{W}{m^2}$. Equation 11 describes a flux of heat out of the far-Eastern Pacific near the coast of Mexico and the United States towards the far-West Pacific, and the two components nearly cancel and so add minimal net heat to the atmosphere.

The representation of the Kuroshio current is made more regional by fluxing heat away from regions of the subtropics where the observed Kuroshio current does not reach. For the region $70^\circ \leq \lambda \leq 240^\circ$ and $-10^\circ \geq \phi \leq 60^\circ$, we specify the parameters in Table 5 applied to equation 5, plus the additional perturbation in equation 12.

$$\nabla \cdot \mathbf{F}_{\text{Kuroshio2}} = \begin{cases} +49.5 \frac{(\lambda - 3\phi - 45^\circ)^2}{2 \cdot 100}) \cdot \exp(-\frac{(\lambda + \phi - 160^\circ)^2}{2 \cdot 20^{\circ 2}}) & , \end{cases} \tag{12}$$

e. Atlantic sector

The representation of the Gulf current is

$$\nabla\cdot\mathbf{F}_{\text{Gulf}}=\begin{cases} 70\frac{W}{m^2}\cdot\exp(-\frac{(\lambda-2\phi-220^\circ)^2}{2\cdot 9})\cdot\exp(-\frac{(\lambda+\phi-335^\circ)^2}{2\cdot 625}) & , \quad 275^\circ\leq\lambda\leq 335^\circ \text{ and } 10^\circ\leq\phi\leq 52^\circ \\ -63.9\frac{W}{m^2}\cdot\exp(-\frac{(\lambda-0.5\phi-325^\circ)^2}{2\cdot 9})\cdot\exp(-\frac{(\phi-25^\circ)^2}{2\cdot 49}) & , \quad 298^\circ\leq\lambda\leq 358^\circ \text{ and } 10^\circ\leq\phi\leq 52^\circ \\ 0 & , \quad \text{otherwise} \end{cases} \tag{13}$$

Equation 13 describes a flux of heat out of the far-Eastern Atlantic towards the far-West Atlantic, and the two components nearly cancel and so add minimal net heat to the atmosphere.

Heat is also fluxed out of the tropical Atlantic and towards the Gulf stream and Norwegian Sea.

$$\nabla\cdot\mathbf{F}_{\text{Atl}}=\begin{cases} -50\frac{W}{m^2}\exp(\frac{-(\lambda-342^\circ)^2}{2\cdot 9^{\circ 2}})\cdot\exp(\frac{-(\phi+5^\circ)^2}{2\cdot 5^{\circ 2}}) & , \quad 275^\circ\leq\lambda\leq 18^\circ \text{ and } -35^\circ\leq\phi\leq 77^\circ \\ -50\frac{W}{m^2}\exp(\frac{-(\lambda-0^\circ)^2}{2\cdot 8^{\circ 2}})\cdot\exp(\frac{-(\phi+5^\circ)^2}{2\cdot 5^{\circ 2}}) & , \quad 275^\circ\leq\lambda\leq 18^\circ \text{ and } -35^\circ\leq\phi\leq 77^\circ \\ -12.6\frac{W}{m^2}\cdot\exp(\frac{-(\lambda-345^\circ)^2}{2\cdot 16^{\circ 2}})\cdot\exp(\frac{-(\phi+16^\circ)^2}{2\cdot 8^{\circ 2}}) & , \quad 275^\circ\leq\lambda \text{ and } -35^\circ\leq\phi\leq 77^\circ \\ +54.7\frac{W}{m^2}\exp(\frac{-(\lambda-2\phi-220^\circ)^2}{2\cdot 100})\cdot\exp(\frac{-(\lambda+\phi-375^\circ)^2}{2\cdot 900}) & , \quad 275^\circ\leq\lambda \text{ and } -35^\circ\leq\phi\leq 77^\circ \\ +64.3\frac{W}{m^2}\cdot\cos(3\cdot(\lambda-348^\circ))\cdot(1-\frac{(\phi-67)}{10^\circ}^4) & , \quad 318^\circ\leq\lambda\leq 18^\circ \text{ and } 57^\circ\leq\phi\leq 77^\circ \\ 0 & , \quad \text{otherwise} \end{cases} \tag{14}$$

In order to avoid strong oceanic heat flux over regions that are actually continents, we modify the heat flux over South America as follows. Over the region $250^\circ\leq\lambda\leq 344^\circ$ and $-35^\circ\leq\phi\leq 40^\circ$, we specify the parameters in Table 6 applied to equation 5. The net effect of this is to flux heat out of the subtropical South America and also out of the subtropical North Atlantic, and converge heat into the Caribbean Sea and towards equatorial South America that otherwise have heat fluxed away due to Equation 9 and 14. The components nearly cancel and so add minimal net heat to the atmosphere.

In order to represent the Brazil and Falkland Current, a dipole is added in the South Atlantic. Over the the region $290° \leq \lambda$ and $-61° \leq \phi \leq -30°$, we specify the parameters in Table 7 applied to equation 5.

Additional heat is fluxed towards the Norwegian and Barents Sea and away from land gridpoints in subtropical Africa as follows:

$$\nabla \cdot \mathbf{F}_{\text{Barents1}} = \begin{cases} 68.0\frac{W}{m^2}(1-(\frac{\phi-76°}{6.5°})^4)\cdot\cos(2(\lambda-30°)) & , \quad 345° \leq \lambda \leq 75° \text{ and } 71° \leq \phi \leq 83° \\ -14.5\frac{W}{m^2}\cdot\exp(\frac{-(\lambda-357°)^2}{2\cdot 400})\cdot\exp(\frac{-(\phi-20°)^2}{2\cdot 7°^2}) & , \quad 310° \leq \lambda \leq 30° \text{ and } 10° \leq \phi \leq 35° \\ 0 & , \quad \text{otherwise} \end{cases} \tag{15}$$

The components nearly cancel and so add minimal net heat to the atmosphere.

The representation of heat uptake in subpolar latitudes is further modified as follows

$$\nabla \cdot \mathbf{F}_{\text{pole}} = \begin{cases} 25.0\frac{W}{m^2}(1-(\frac{\phi-76°}{7°})^4)\cdot\cos(\lambda-10°) & , \quad 69° \leq \phi \leq 83° \\ 68.2\frac{W}{m^2}(1-(\frac{\phi-68°}{8°})^4)\cdot\cos(6(\lambda-2°)) & , \quad 347° \leq \lambda \leq 17° \text{ and } 60° \leq \phi \leq 76° \\ -38\frac{W}{m^2}\exp(\frac{-(\lambda-2\phi-152°)^2}{2\cdot 100})\exp(\frac{-(\lambda+\phi-342°)^2}{2\cdot 20°^2}) & , \quad 260° \leq \lambda \leq 310° \text{ and } 55° \leq \phi \leq 85° \\ -100\frac{W}{m^2}\exp(\frac{-(\lambda-275°)^2}{2\cdot 25})\exp(\frac{-(\phi-58°)^2}{2\cdot 4°^2}) & , \quad 260° \leq \lambda \leq 310° \text{ and } 55° \leq \phi \leq 85° \\ 10.8\frac{W}{m^2}\exp(\frac{-(\lambda-2\phi-220°)^2}{2\cdot 100})\exp(\frac{-(\lambda+\phi-335°)^2}{2\cdot 625}) & , \quad 275° \leq \lambda \leq 335° \text{ and } 10° \geq \phi \leq 52° \\ 0 & , \quad \text{otherwise} \end{cases} \tag{16}$$

The components nearly cancel and so add minimal net heat to the atmosphere. This specification represents a divergence of heat away from the Chukchi and Beaufort seas and Hudson Bay and Baffin Bay, and convergence in the Norwegian and Barents Sea, in order to better capture the pattern of surface temperature. Note that we specify a zonally symmetric albedo, while in reality, sea ice coverage is less extensive in the Norwegian and Barents Seas as compared to similar latitudes elsewhere.

Acknowledgments. CIG, IW, and ME acknowledge the support of a European Research Council starting grant under the European Union Horizon 2020 research and innovation programme (grant agreement number 677756). EPG acknowledges support from the US NSF through grant AGS-1852727. MJ acknowledges support from the Australian Research Council (ARC) Centre of Excellence for Climate Extremes (CE170100023) and ARC grant FL 150100035. We thank Ori Adam for helpful comments on an earlier version of this manuscript. Code for this model configuration will be made available on GitHub as part of the MiMA v2.0 release.

References

, 2010: SPARC CCMVal Report on the Evaluation of Chemistry-Climate Models. Tech. rep., SPARC, 426 pp. pp. URL http://www.sparc-climate.org/publications/sparc-reports/.

AchutaRao, K., and K. R. Sperber, 2006: Enso simulation in coupled ocean-atmosphere models: are the current models better? *Climate Dynamics*, **27 (1)**, 1–15.

Adam, O., T. Schneider, and F. Brient, 2018: Regional and seasonal variations of the double-itcz bias in cmip5 models. *Climate dynamics*, **51 (1-2)**, 101–117.

Adam, O., T. Schneider, F. Brient, and T. Bischoff, 2016: Relation of the double-itcz bias to the atmospheric energy budget in climate models. *Geophysical Research Letters*, **43 (14)**, 7670–7677.

Adler, R. F., and Coauthors, 2003: The Version-2 Global Precipitation Climatology Project (GPCP) Monthly Precipitation Analysis (1979 Present). *Journal of Hydrometeorology*, **4**, 1147, doi:10.1175/1525-7541(2003)004⟨1147:TVGPCP⟩2.0.CO;2.

Alexander, M., and T. Dunkerton, 1999: A spectral parameterization of mean-flow forcing due to breaking gravity waves. *Journal of the atmospheric sciences*, **56 (24)**, 4167–4182, doi:10.1175/1520-0469(1999)056⟨4167:ASPOMF⟩2.0.CO;2.

Bayr, T., D. I. Domeisen, and C. Wengel, 2019: The effect of the equatorial pacific cold sst bias on simulated enso teleconnections to the north pacific and california. *Climate Dynamics*, 1–19.

Bellenger, H., É. Guilyardi, J. Leloup, M. Lengaigne, and J. Vialard, 2014: Enso representation in climate models: from cmip3 to cmip5. *Climate Dynamics*, **42 (7-8)**, 1999–2018.

Betts, A., and M. Miller, 1986: A new convective adjustment scheme. part ii: Single column tests using gate wave, bomex, atex and arctic air-mass data sets. *Quarterly Journal of the Royal Meteorological Society*, **112 (473)**, 693–709, doi:10.1002/qj.49711247308.

Betts, A. K., 1986: A new convective adjustment scheme. part i: Observational and theoretical basis. *Quarterly Journal of the Royal Meteorological Society*, **112 (473)**, 677–691, doi:10.1002/qj.49711247307.

Bracegirdle, T. J., E. Shuckburgh, J.-B. Sallee, Z. Wang, A. J. Meijers, N. Bruneau, T. Phillips, and L. J. Wilcox, 2013: Assessment of surface winds over the atlantic, indian, and pacific ocean sectors of the southern ocean in cmip5 models: Historical bias, forcing response, and state dependence. *Journal of Geophysical Research: Atmospheres*, **118 (2)**, 547–562.

Ceppi, P., Y.-T. Hwang, D. M. Frierson, and D. L. Hartmann, 2012: Southern hemisphere jet latitude biases in cmip5 models linked to shortwave cloud forcing. *Geophysical Research Letters*, **39 (19)**.

Cohen, N. Y., E. P. Gerber, and E. P. Oliver Bühler, 2013: Compensation between resolved and unresolved wave driving in the stratosphere: Implications for downward control. *Journal of the Atmospheric Sciences*, **70 (12)**, 3780–3798, doi:10.1175/JAS-D-12-0346.1.

Forget, G., and D. Ferreira, 2019: Global ocean heat transport dominated by heat export from the tropical pacific. *Nature Geoscience*, **12 (5)**, 351.

Frierson, D. M., I. M. Held, and P. Zurita-Gotor, 2006: A gray-radiation aquaplanet moist gcm. part i: Static stability and eddy scale. *Journal of the atmospheric sciences*, **63 (10)**, 2548–2566, doi:10.1175/JAS3753.1.

Frierson, D. M., I. M. Held, and P. Zurita-Gotor, 2007: A gray-radiation aquaplanet moist gcm. part ii: Energy transports in altered climates. *Journal of the atmospheric sciences*, **64 (5)**, 1680–1693, doi:10.1175/JAS3913.1.

Garfinkel, C., L. D. Oman, E. A. Barnes, D. W. Waugh, M. M. Hurwitz, and A. M. Molod, 2013a: Connections between the spring breakup of the southern hemisphere polar vortex, stationary waves, and air-sea roughness. *J. Atmos. Sci.*, **70**, 2137–2151, doi:http://dx.doi.org/10.1175/JAS-D-12-0242.1.

Garfinkel, C. I., O. Adam, E. Morin, Y. Enzel, E. Elbaum, M. Bartov, D. Rostkier-Edelstein, and U. Dayan, 2020a: The role of zonally averaged climate change in contributing to intermodel spread in cmip5 predicted local precipitation changes. *Journal of Climate*, doi:10.1175/JCLI-D-19-0232.1.

Garfinkel, C. I., D. W. Waugh, and E. P. Gerber, 2013b: The effect of tropospheric jet latitude on coupling between the stratospheric polar vortex and the troposphere. *Journal of Climate*, **26 (6)**, doi:10.1175/JCLI-D-12-00301.1.

Garfinkel, C. I., I. P. White, E. P. Gerber, and M. Jucker, 2020b: The building blocks of northern hemisphere wintertime stationary waves. *Journal of Climate*, **in press**, doi:10.1175/JCLI-D-19-0181.1.

He, J., and B. J. Soden, 2016: The impact of sst biases on projections of anthropogenic climate change: A greater role for atmosphere-only models? *Geophysical Research Letters*, **43 (14)**, 7745–7750.

Held, I. M., and B. J. Soden, 2006: Robust responses of the hydrological cycle to global warming. *Journal of climate*, **19 (21)**, 5686–5699.

Holton, L., J. Deshayes, B. Backeberg, B. Loveday, J. Hermes, and C. Reason, 2017: Spatio-temporal characteristics of agulhas leakage: a model inter-comparison study. *Climate dynamics*, **48 (7-8)**, 2107–2121.

Hubert, L., A. Krueger, and J. Winston, 1969: The double intertropical convergence zone-fact or fiction? *Journal of the Atmospheric Sciences*, **26 (4)**, 771–773.

Hwang, Y.-T., and D. M. Frierson, 2013: Link between the double-intertropical convergence zone problem and cloud biases over the southern ocean. *Proceedings of the National Academy of Sciences*, **110 (13)**, 4935–4940.

Iacono, M. J., E. J. Mlawer, S. A. Clough, and J.-J. Morcrette, 2000: Impact of an improved longwave radiation model, rrtm, on the energy budget and thermodynamic properties of the ncar community climate model, ccm3. *Journal of Geophysical Research: Atmospheres*, **105 (D11)**, 14 873–14 890.

Inatsu, M., and B. J. Hoskins, 2004: The zonal asymmetry of the southern hemisphere winter storm track. *Journal of climate*, **17 (24)**, 4882–4892.

James, I., 1988: On the forcing of planetary-scale rossby waves by antarctica. *Quarterly Journal of the Royal Meteorological Society*, **114 (481)**, 619–637.

Jucker, M., 2017: mjucker/mima: Mima v1.0. **Accessed 2017**, doi:https://doi.org/10.5281/zenodo.321708.

Jucker, M., 2019: The surface of an aquaplanet gcm. doi:10.5281/zenodo.3358284.

Jucker, M., and E. Gerber, 2017: Untangling the annual cycle of the tropical tropopause layer with an idealized moist model. *Journal of Climate*, **30 (18)**, 7339–7358.

Kay, J. E., C. Wall, V. Yettella, B. Medeiros, C. Hannay, P. Caldwell, and C. Bitz, 2016: Global climate impacts of fixing the southern ocean shortwave radiation bias in the community earth system model (cesm). *Journal of Climate*, **29 (12)**, 4617–4636.

Kidston, J., and E. P. Gerber, 2010: Intermodel variability of the poleward shift of the austral jet stream in the CMIP3 integrations linked to biases in 20th century climatology. *Geophys. Res. Lett.*, **37**, L09 708, doi:10.1029/2010GL042873.

Knutti, R., and J. Sedláček, 2013: Robustness and uncertainties in the new cmip5 climate model projections. *Nature Climate Change*, **3 (4)**, 369.

Kwon, Y.-O., M. A. Alexander, N. A. Bond, C. Frankignoul, H. Nakamura, B. Qiu, and L. A. Thompson, 2010: Role of the gulf stream and kuroshio–oyashio systems in large-scale atmosphere–ocean interaction: A review. *Journal of Climate*, **23 (12)**, 3249–3281.

Li, G., and S.-P. Xie, 2014: Tropical biases in cmip5 multimodel ensemble: The excessive equatorial pacific cold tongue and double itcz problems. *Journal of Climate*, **27 (4)**, 1765–1780.

Li, G., S.-P. Xie, Y. Du, and Y. Luo, 2016: Effects of excessive equatorial cold tongue bias on the projections of tropical pacific climate change. part i: The warming pattern in cmip5 multi-model ensemble. *Climate dynamics*, **47 (12)**, 3817–3831.

Lin, J.-L., 2007: The double-itcz problem in ipcc ar4 coupled gcms: Ocean–atmosphere feedback analysis. *Journal of Climate*, **20 (18)**, 4497–4525.

Lindberg, C., and A. J. Broccoli, 1996: Representation of topography in spectral climate models and its effect on simulated precipitation. *Journal of Climate*, **9 (11)**, 2641–2659.

Liu, W. T., X. Xie, and P. P. Niiler, 2007: Ocean–atmosphere interaction over agulhas extension meanders. *Journal of climate*, **20 (23)**, 5784–5797.

Luo, J.-J., S. Masson, E. Roeckner, G. Madec, and T. Yamagata, 2005: Reducing climatology bias in an ocean–atmosphere cgcm with improved coupling physics. *Journal of climate*, **18 (13)**, 2344–2360.

Lutjeharms, J., 2007: Three decades of research on the greater agulhas current. *Ocean Science*, **3 (1)**, 129–147.

Matsueda, M., and T. N. Palmer, 2011: Accuracy of climate change predictions using high resolution simulations as surrogates of truth. *Geophysical Research Letters*, **38 (5)**, doi: 10.1029/2010GL046618.

Mbengue, C., and T. Schneider, 2017: Storm-track shifts under climate change: Toward a mechanistic understanding using baroclinic mean available potential energy. *Journal of the Atmospheric Sciences*, **74 (1)**, 93–110.

Mechoso, C. R., and Coauthors, 1995: The seasonal cycle over the tropical pacific in coupled ocean–atmosphere general circulation models. *Monthly Weather Review*, **123 (9)**, 2825–2838.

Merlis, T. M., T. Schneider, S. Bordoni, and I. Eisenman, 2013: Hadley circulation response to orbital precession. part ii: Subtropical continent. *Journal of Climate*, **26 (3)**, 754–771.

Minobe, S., A. Kuwano-Yoshida, N. Komori, S.-P. Xie, and R. J. Small, 2008: Influence of the gulf stream on the troposphere. *Nature*, **452 (7184)**, 206.

Mlawer, E. J., S. J. Taubman, P. D. Brown, M. J. Iacono, and S. A. Clough, 1997: Radiative transfer for inhomogeneous atmospheres: Rrtm, a validated correlated-k model for the longwave. *Journal of Geophysical Research: Atmospheres*, **102 (D14)**, 16 663–16 682.

Ogawa, F., N.-E. Omrani, K. Nishii, H. Nakamura, and N. Keenlyside, 2015: Ozone-induced climate change propped up by the southern hemisphere oceanic front. *Geophysical Research Letters*, **42 (22)**, 10–056.

Peña-Ortiz, C., E. Manzini, and M. A. Giorgetta, 2019: Tropical deep convection impact on southern winter stationary waves and its modulation by the quasi-biennial oscillation. *Journal of Climate*, **32 (21)**, 7453–7467.

Quintanar, A. I., and C. R. Mechoso, 1995a: Quasi-stationary waves in the southern hemisphere. part i: Observational data. *Journal of Climate*, **8 (11)**, 2659–2672.

Quintanar, A. I., and C. R. Mechoso, 1995b: Quasi-stationary waves in the southern hemisphere. part ii: Generation mechanisms. *Journal of climate*, **8 (11)**, 2673–2690.

Sampe, T., H. Nakamura, A. Goto, and W. Ohfuchi, 2010: Significance of a midlatitude sst frontal zone in the formation of a storm track and an eddy-driven westerly jet. *Journal of Climate*, **23 (7)**, 1793–1814.

Sardeshmukh, P. D., and B. J. Hoskins, 1988: The generation of global rotational flow by steady idealized tropical divergence. *J. Atmos. Sci.*, **45**, 1228–1251.

Scheff, J., and D. Frierson, 2012: Twenty-first-century multimodel subtropical precipitation declines are mostly midlatitude shifts. *Journal of Climate*, **25 (12)**, 4330–4347.

Scott, R. K., and P. H. Haynes, 2002: The seasonal cycle of planetary waves in the winter stratosphere. *J. Atmos. Sci.*, **59**, 803–822, doi:10.1175/1520-0469(2002)059.

Seviour, W. J., D. W. Waugh, L. M. Polvani, G. J. Correa, and C. I. Garfinkel, 2017: Robustness of the simulated tropospheric response to ozone depletion. *Journal of Climate*, **30 (7)**, 2577–2585.

Shaw, T., and Coauthors, 2016: Storm track processes and the opposing influences of climate change. *Nature Geoscience*, **9 (9)**, 656.

Sigmond, M., and J. C. Fyfe, 2014: The antarctic sea ice response to the ozone hole in climate models. *Journal of Climate*, **27 (3)**, 1336–1342.

Simpson, I. R., T. A. Shaw, and R. Seager, 2014: A diagnosis of the seasonally and longitudinally varying midlatitude circulation response to global warming. *Journal of the Atmospheric Sciences*, **71 (7)**, 2489–2515.

Small, R. J., R. A. Tomas, and F. O. Bryan, 2014: Storm track response to ocean fronts in a global high-resolution climate model. *Climate dynamics*, **43 (3-4)**, 805–828.

Son, S.-W., and Coauthors, 2018: Tropospheric jet response to antarctic ozone depletion: An update with chemistry-climate model initiative (ccmi) models. *Environmental Research Letters*, **13 (5)**, 054 024.

Swart, N., and J. Fyfe, 2012a: Observed and simulated changes in the southern hemisphere surface westerly wind-stress. *Geophysical Research Letters*, **39 (16)**, doi:10.1029/2012GL052810.

Swart, N., and J. Fyfe, 2012b: Ocean carbon uptake and storage influenced by wind bias in global climate models. *Nature Climate Change*, **2 (1)**, 47.

Takahashi, K., and D. S. Battisti, 2007: Processes controlling the mean tropical pacific precipitation pattern. part ii: The spcz and the southeast pacific dry zone. *Journal of Climate*, **20 (23)**, 5696–5706.

Taylor, K. E., R. J. Stouffer, and G. A. Meehl, 2012: An overview of cmip5 and the experiment design. *Bulletin of the American Meteorological Society*, **93 (4)**, 485–498.

Trenberth, K. E., and J. T. Fasullo, 2018: Applications of an updated atmospheric energetics formulation. *Journal of Climate*, **31 (16)**, 6263–6279, doi:10.1175/JCLI-D-17-0838.1.

Trenberth, K. E., Y. Zhang, J. T. Fasullo, and L. Cheng, 2019: Observation-based estimate of global and basin ocean meridional heat transport time series. *Journal of Climate*, **32**, doi:10.1175/JCLI-D-18-0872.1.

Wang, L., P. J. Kushner, and D. W. Waugh, 2013: Southern hemisphere stationary wave response to changes of ozone and greenhouse gases. *Journal of climate*, **26 (24)**, 10 205–10 217.

Watanabe, S., and Coauthors, 2011: Miroc-esm 2010: Model description and basic results of cmip5-20c3m experiments. *Geoscientific Model Development*, **4 (4)**, 845.

Weijer, W., and Coauthors, 2012: The southern ocean and its climate in ccsm4. *Journal of Climate*, **25 (8)**, 2652–2675.

Wilcox, L., A. Charlton-Perez, and L. Gray, 2012: Trends in austral jet position in ensembles of high-and low-top cmip5 models. *Journal of Geophysical Research: Atmospheres (1984–2012)*, **117 (D13)**, doi:10.1029/2012JD017597.

Wills, R. C., and T. Schneider, 2018: Mechanisms setting the strength of orographic rossby waves across a wide range of climates in a moist idealized gcm. *Journal of Climate*, **31 (18)**, 7679–7700.

Wirth, V., 1991: What causes the seasonal cycle of stationary waves in the southern stratosphere? *J. Atmos. Sci.*, **48**, 1194–1200, doi:10.1175/1520-0469(1991)048.

Xiang, B., M. Zhao, I. M. Held, and J.-C. Golaz, 2017: Predicting the severity of spurious "double itcz" problem in cmip5 coupled models from amip simulations. *Geophysical Research Letters*, **44 (3)**, 1520–1527.

Xu, H., M. Xu, S.-P. Xie, and Y. Wang, 2011: Deep atmospheric response to the spring kuroshio over the east china sea. *Journal of climate*, **24 (18)**, 4959–4972.

Yao, Y., Z. Zhong, and X.-Q. Yang, 2016: Numerical experiments of the storm track sensitivity to oceanic frontal strength within the kuroshio/oyashio extensions. *Journal of Geophysical Research: Atmospheres*, **121 (6)**, 2888–2900.

Zhang, C., 2001: Double itczs. *Journal of Geophysical Research: Atmospheres*, **106 (D11)**, 11 785–11 792.

Zhang, G. J., and H. Wang, 2006: Toward mitigating the double itcz problem in ncar ccsm3. *Geophysical research letters*, **33 (6)**.

LIST OF TABLES

TABLE 1. list of models used

1	ACCESS1-0	2	ACCESS1-3	3	BNU-ESM
4	CCSM4	5	CESM1-BGC	6	CESM1-CAM5
7	CESM1-FASTCHEM	8	CESM1-WACCM	9	CMCC-CESM
10	CMCC-CM	11	CMCC-CMS	12	CNRM-CM5
13	CNRM-CM5-2	14	CSIRO-Mk3-6-0	15	CanCM4
16	CanESM2	17	FGOALS-g2	18	FIO-ESM
19	GFDL-CM2p1	20	GFDL-CM3	21	GFDL-ESM2G
22	GFDL-ESM2M	23	GISS-E2-H	24	GISS-E2-H-CC
25	GISS-E2-R	26	GISS-E2-R-CC	27	HadCM3
28	HadGEM2-AO	29	IPSL-CM5A-LR	30	IPSL-CM5A-MR
31	IPSL-CM5B-LR	32	MIROC-ESM	33	MIROC-ESM-CHEM
34	MIROC4h	35	MIROC5	36	MPI-ESM-LR
37	MPI-ESM-MR	38	MPI-ESM-P	39	MRI-CGCM3
40	MRI-ESM1	41	NorESM1-M	42	NorESM1-ME
43	bcc-csm1-1	44	bcc-csm1-1-m	45	inmcm4

TABLE 2. parameters for the Agulhas following Equation 5

A_n ($\frac{W}{m^2}$)	$\mu_{\lambda n}$ (° longitude)	$\sigma_{\lambda n}$ (° longitude)	$\mu_{\phi n}$ (° latitude)	$\sigma_{\phi n}$ (° latitude)
-30	28	10	18	$\sqrt{50}$
-30	28	10	-18	$\sqrt{60}$
-(38.5+Africaextra*0.7709)	11	2	-15	10
+(83+Africaextra)	50	25	-40	4
-(64.22+Africaextra*1.3)	50	20	-48	4
+20	14	$\sqrt{30}$	0	$\sqrt{50}$
+11	36	$\sqrt{30}$	0	$\sqrt{50}$

TABLE 3. parameters for the Cold Tongue following Equation 5

A_n ($\frac{W}{m^2}$)	$\mu_{\lambda n}$ ($^\circ$ longitude)	$\sigma_{\lambda n}$ ($^\circ$ longitude)	$\mu_{\phi n}$ ($^\circ$ latitude)	$\sigma_{\phi n}$ ($^\circ$ latitude)
-(50-ITCZEW*0.28)	270	9	0	3
-(50-ITCZEW*0.28)	250	9	-1	3
-(50-ITCZEW*0.28)	230	9	-2	3
-39	210	9	-2	3
-36	190	9	0	3
-16	170	9	0	3
-40	287	2	-25	9
-15	282	5	-15	9
-(25.+ ITCZNS+ITCZEW)	240	40	-21	11
-38	195	13	16	7
-51.4	225	13	16	7
+(28.2+ ITCZNS*.8623)	220	40	-57	15
+(14+ ITCZEW*1.1195)	165	20	-20	5
+(16+ ITCZEW*1.1195)	195	20	-33	7
+(50+ ITCZEW*1.1195)	155	3	-30	7
+(40+ ITCZEW*1.1195)	180	5	-40	5
+(41+ ITCZNS)	240	30	-62	8
+60	180	13	6.97	2
+47	210	13	6.97	2
+45	240	13	6.97	2
+(19.5+ITCZEW)	145	14	3	4
+(40+ITCZEW*.435)	150	13	7	3

TABLE 4. parameters for Australia following Equation 5

A_n ($\frac{W}{m^2}$)	$\mu_{\lambda n}$ (° longitude)	$\sigma_{\lambda n}$ (° longitude)	$\mu_{\phi n}$ (° latitude)	$\sigma_{\phi n}$ (° latitude)
-1.02(Q_{Pacific}+Q_o)	135	225	-20	6
-10	147	64	-27	7
+16.6	120	900	-20	6
+27.89	100	100	-10	4
+4.9	135	225	0	4

TABLE 5. parameters for Kuroshio following Equation 5

A_n ($\frac{W}{m^2}$)	$\mu_{\lambda n}$ ($^\circ$ longitude)	$\sigma_{\lambda n}$ ($^\circ$ longitude)	$\mu_{\phi n}$ ($^\circ$ latitude)	$\sigma_{\phi n}$ ($^\circ$ latitude)
-27.60	140	39	19.7	7
-5.2	140	8	20	4
+35.4	160	20	35	6
+22.9	90	12	0	5

TABLE 6. parameters for South America following Equation 5

A_n ($\frac{W}{m^2}$)	$\mu_{\lambda n}$ ($^\circ$ longitude)	$\sigma_{\lambda n}$ ($^\circ$ longitude)	$\mu_{\phi n}$ ($^\circ$ latitude)	$\sigma_{\phi n}$ ($^\circ$ latitude)
-0.92Q_o	290	20	-20	7
-16.8	325	22	19.5	8
+1.2Q_o	270	7	22	5
+1.58Q_o	283	5	0	6
+1.06415Q_o	304	6	-2	7
+0.85Q_o	284	5	-10	6
+0.63Q_o	317	5	-6	4
+42.54	325	11	+4.2	2

TABLE 7. parameters for the South Atlantic following Equation 5

A_n ($\frac{W}{m^2}$)	$\mu_{\lambda n}$ ($^\circ$ longitude)	$\sigma_{\lambda n}$ ($^\circ$ longitude)	$\mu_{\phi n}$ ($^\circ$ latitude)	$\sigma_{\phi n}$ ($^\circ$ latitude)
+37.4	323	11	-36	4
-40	311	11	-45	4

LIST OF FIGURES

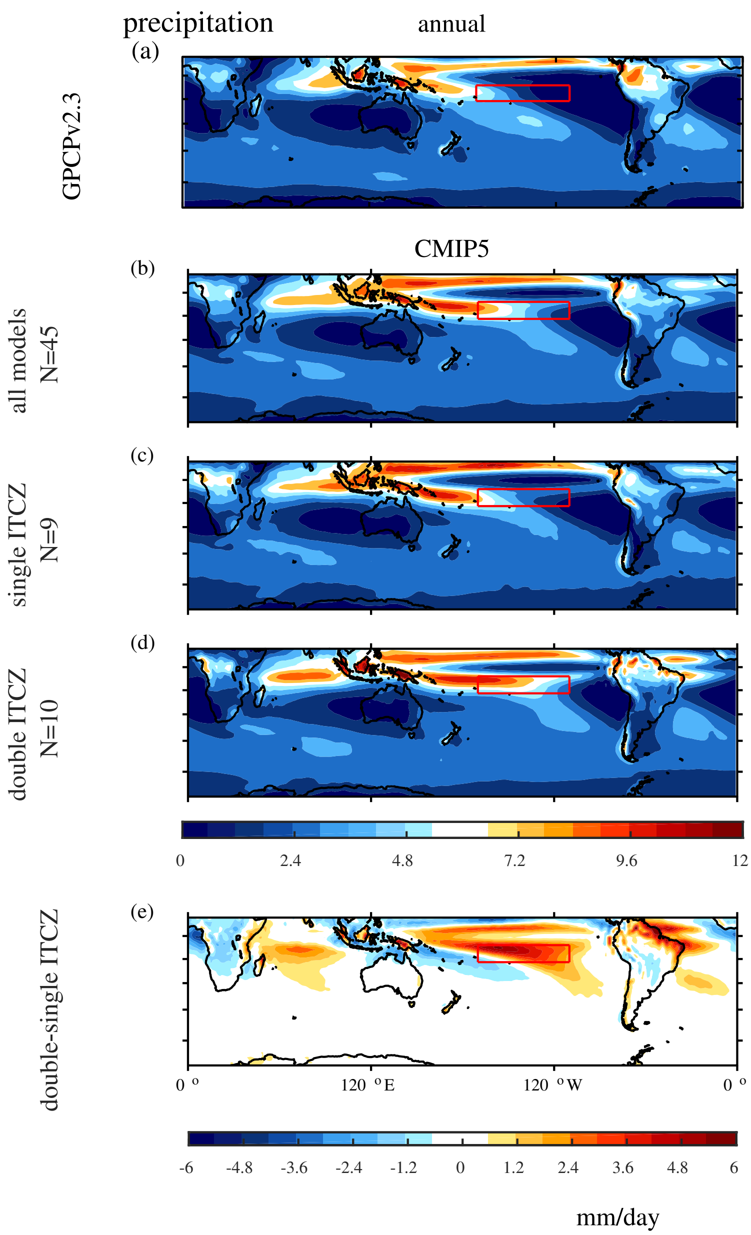

FIG. 1. (a) Climatology of precipitation in GPCP data [mm/day] in the annual average. (b) as in (a) but in the 45 CMIP5 listed in Table 1; (c) in models with a relatively small double ITCZ bias, defined here as simulating precipitation in the region 17S to 2S, 190E to 250E less than 175% of the observed value (excluding MIROC models), (d) in models with a relatively large double ITCZ bias, defined here as simulating more than 250% of the observed value of precipitation in the region 17S to 2S, 190E to 250E ; (e) difference between (d) and (c) (i.e. d-c). The contour interval is 1.2mm/day for (a)-(d) and 0.6mm/day for (e).

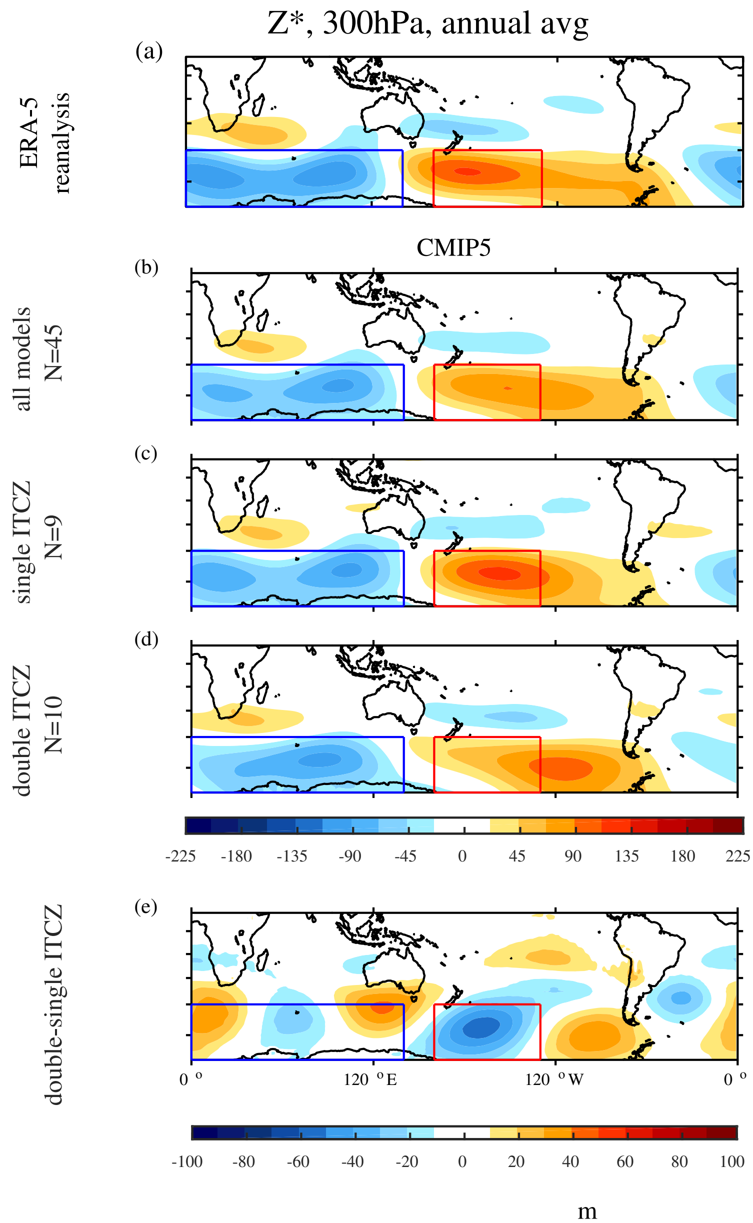

925 FIG. 2. As in Figure 1 but for geopotential height at 300hPa. The contour interval is 22.5m for (a)-(d) and
926 10m for (e).

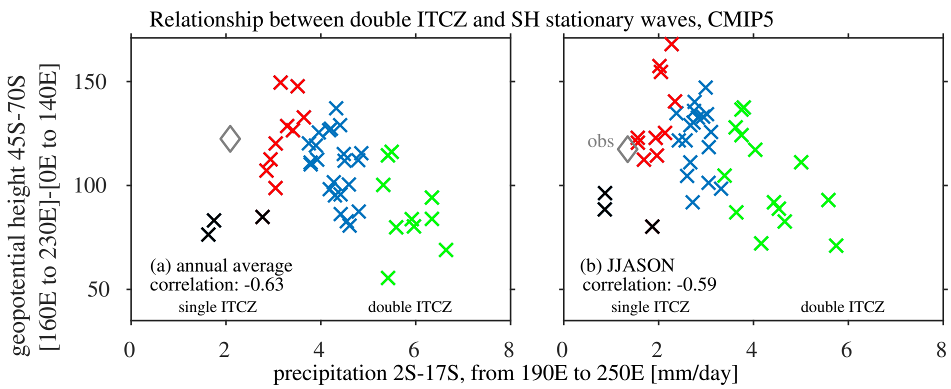

FIG. 3. Relationship between SH 300hPa geopotential height zonal asymmetries and precipitation in the double ITCZ region (17S to 2S, 190E to 250E) in the (a) annual average and in (b) June through November. The models included in Figure 1c and Figure 2c (e.g. less pronounced double-ITCZ models) are shown in red, while the models included in Figure 1d and Figure 2d (e.g. severe double-ITCZ models) are shown in green. Observations (GPCP precipitation and ERA5 heights) are shown with a diamond, and models are shown with an 'x'. Models with precipitation between 175% and 250% of that observed are in blue, and the MIROC models are in black.

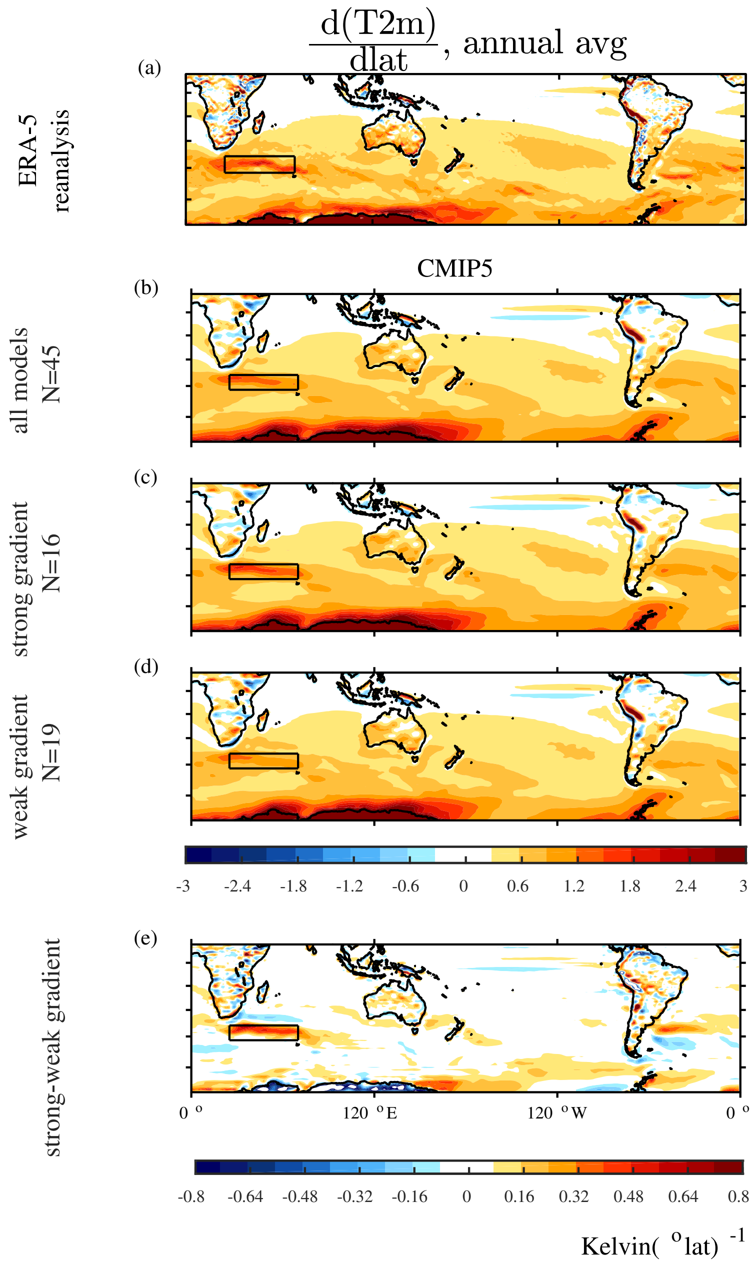

FIG. 4. (a) Climatology of the meridional near-surface temperature gradient in ERA-5 data in the annual average. (b) as in (a) but in the 45 CMIP5 listed in Table 1; (c) in models with a surface temperature gradient in the Agulhas retroflection region (the black-boxed region) at least as strong as that observed, (d) in models with a surface temperature gradient in this region less than 90% of the observed value; (e) difference between (c) and (d). The contour interval is 0.3K(degree latitude)$^{-1}$ for (a)-(d) and 0.08K(degree latitude)$^{-1}$ for (e).

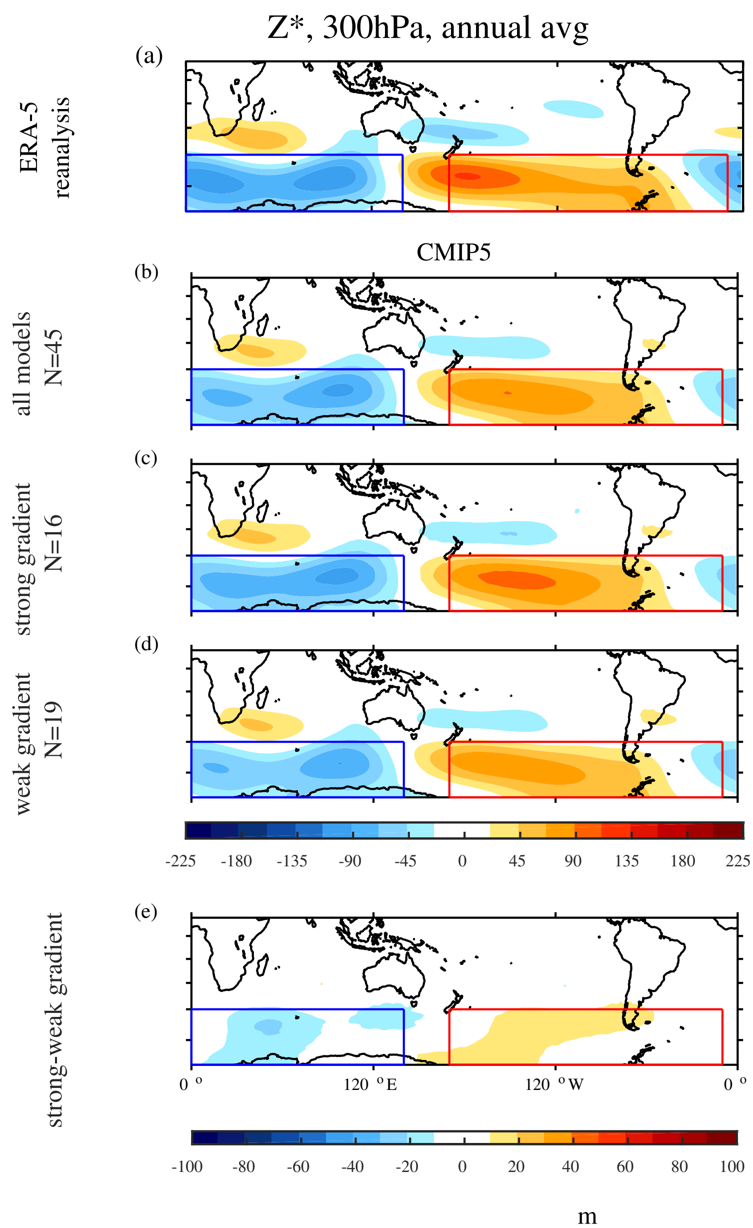

939 FIG. 5. As in Figure 4 but for geopotential height at 300hPa. The contour interval is 22.5m for (a)-(d) and
940 10m for (e).

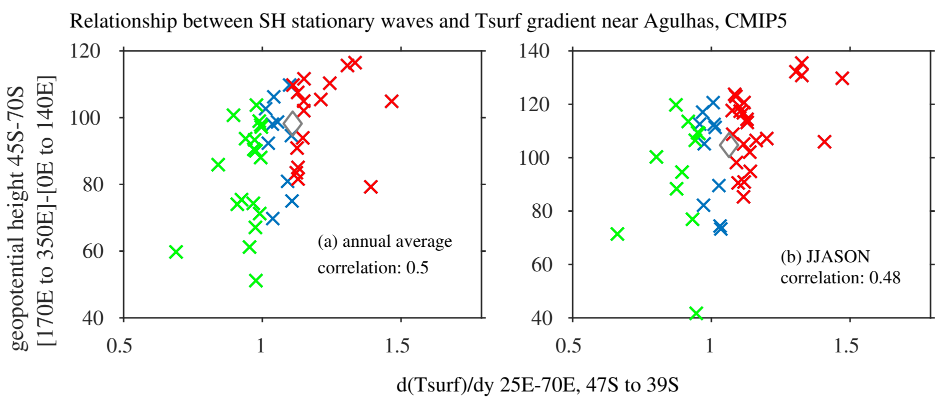

FIG. 6. Relationship between SH 300hPa geopotential height zonal asymmetries and the meridional surface temperature gradient in the Agulhas retroflection region (the black-boxed region on Figure 4) in the (a) annual average and in (b) June through November. The models included in Figure 4c and Figure 5c (e.g. gradient as strong as that observed) are shown in red, while the models included in Figure 4d and Figure 5d (too-weak Agulhas retroflection) are shown in green. Other models are in blue. Reanalysis (ERA5) is shown with a diamond.

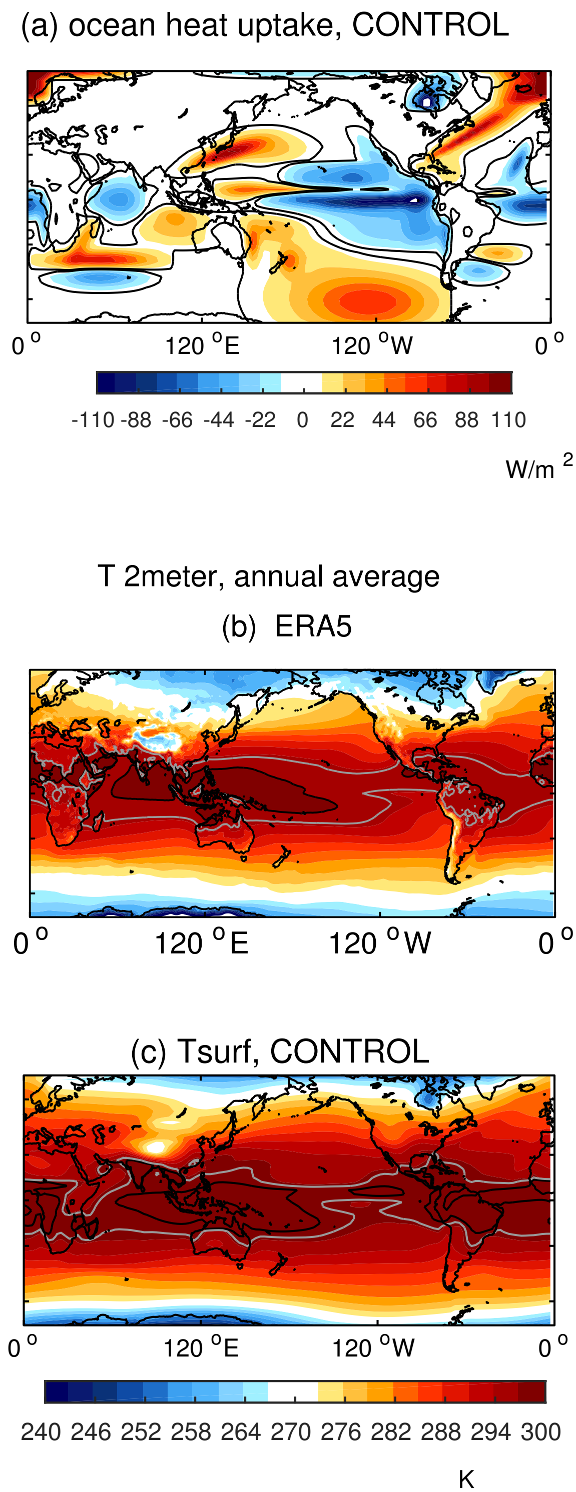

FIG. 7. (a) Ocean heat uptake in W/m^2 in CONTROL. Two reanalysis/satellite based estimate of ocean heat flux can be found in Forget and Ferreira (2019) and Trenberth et al. (2019). Climatology of surface temperature in (b) ERA-5 data and (c) the CONTROL integration in the annual average, with the 298K and 300K isotherms in gray and black.

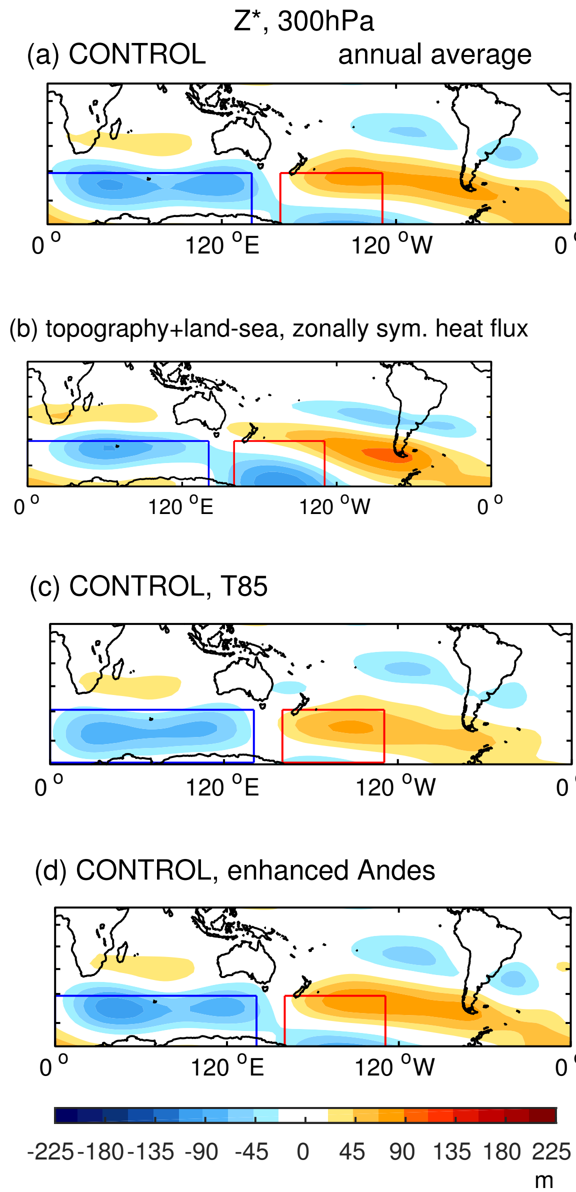

FIG. 8. Zonally asymmetric component of geopotential height at 300hPa in the annual average (a) in the the control integration as detailed in the appendix, (b) in an integration with topography and land-sea contrast as in control but with ocean heat fluxes as specified by equation 4 only; (c) as in (a) but at T85; (d) as in (a) but with the Andes enhanced as described in the text. The contour interval is 22.5m.

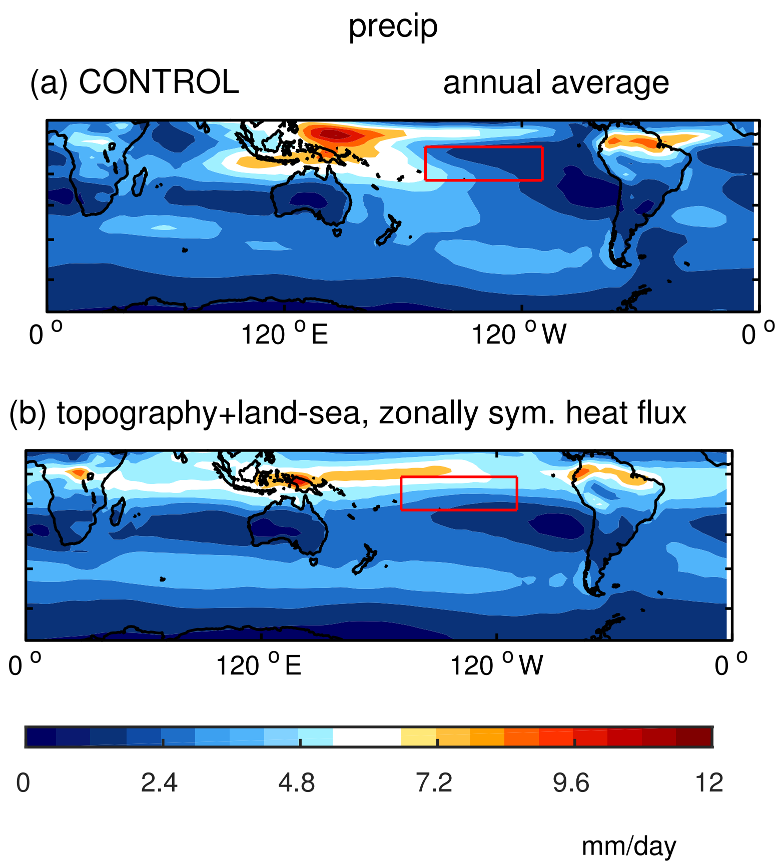

FIG. 9. As in Figure 8a-b but for precipitation. The contour interval is 1.2mm/day.

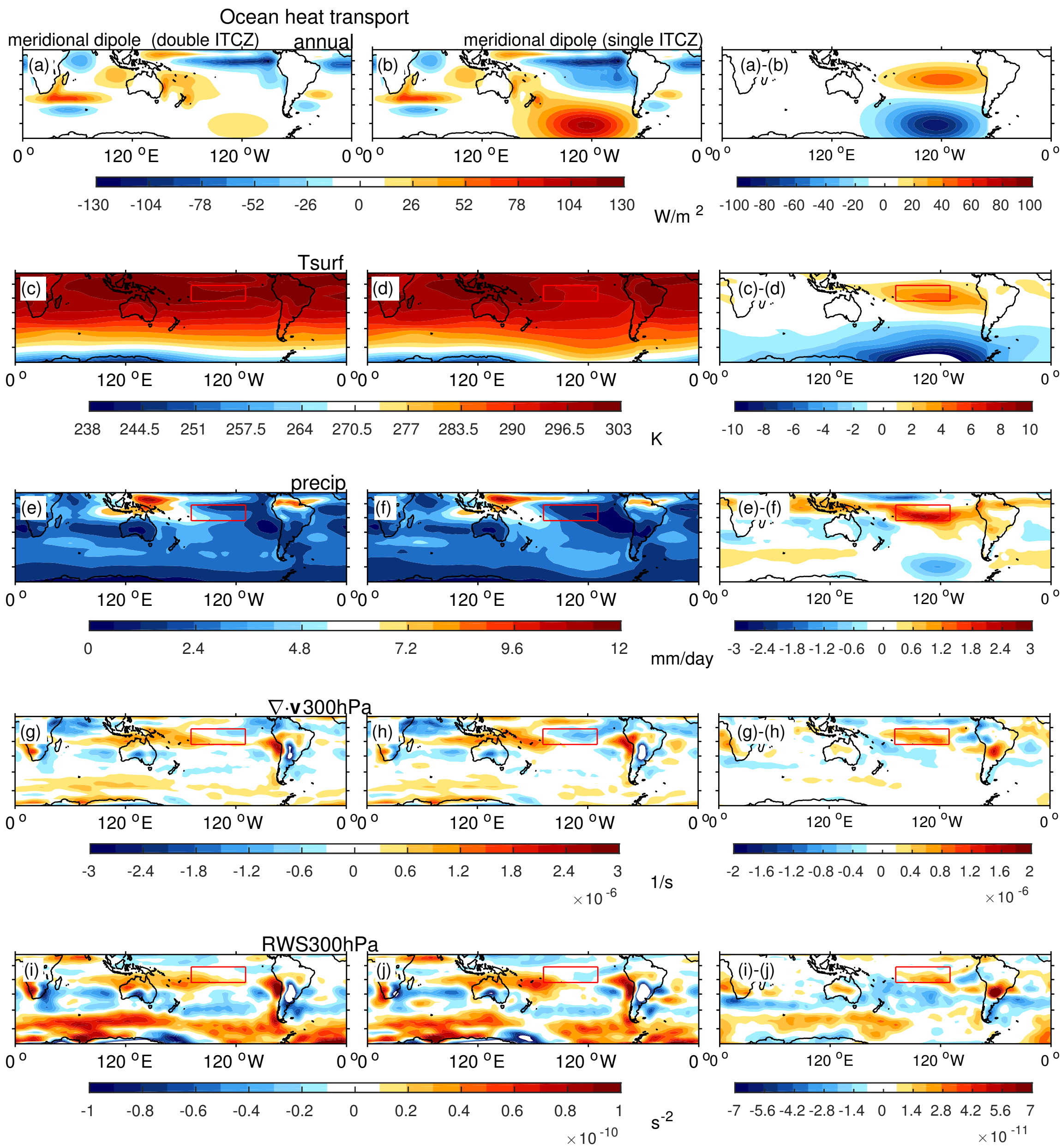

FIG. 10. Annual averaged response to a (left) double ITCZ versus a (middle) single ITCZ, and the (right) difference between the two, with a meridional dipole in the South Pacific allowing or restricting a double ITCZ. (a-b) ocean heat flux; (c-d) surface temperature; (e-f) precipitation.

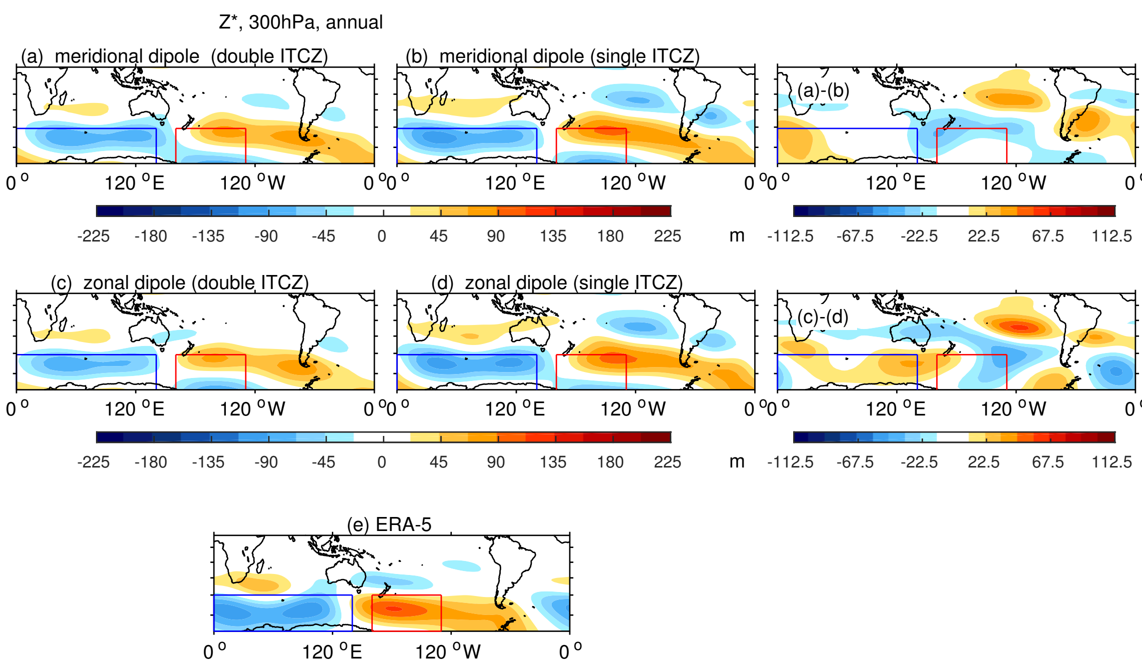

958 FIG. 11. As in Figure 10a-b but for the zonally asymmetric component of the geopotential height at 300hPa; (a) -(b) meridional dipole in the South Pacific so as to allow or restrict a double ITCZ; (c)-(d) zonal dipole in the South Pacific; (e) ERA-5 reanalysis data (repeated from Figures 2a and 5a).

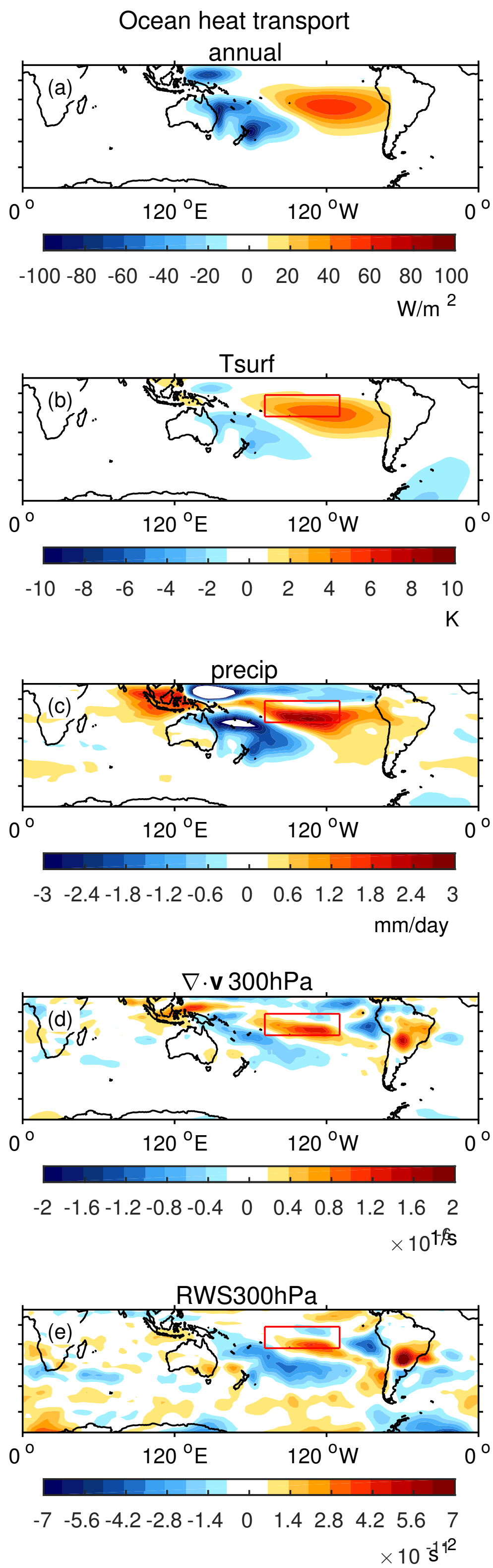

FIG. 12. As in the right column of Figure 10 but for the experiments with a zonal dipole in the South Pacific so as to allow or restrict a double ITCZ.

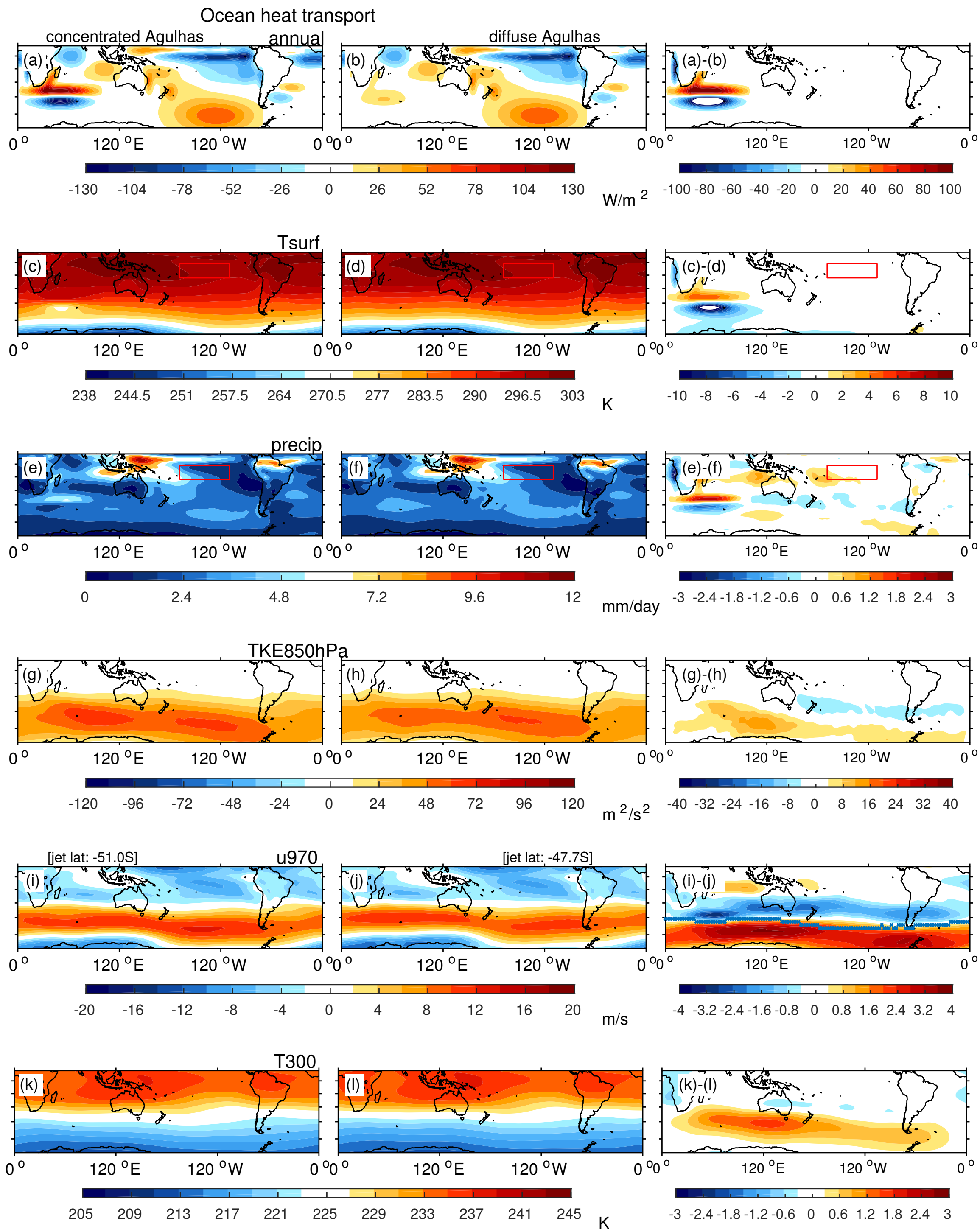

FIG. 13. (a)-(h) As in Figure 12 but for a (left) sharp versus a (middle) diffuse Agulhas Current system. (g-h) transient kinetic energy at 850hPa; (i-j) temperature at 300hPa; (k-l) zonal wind at 970hPa.

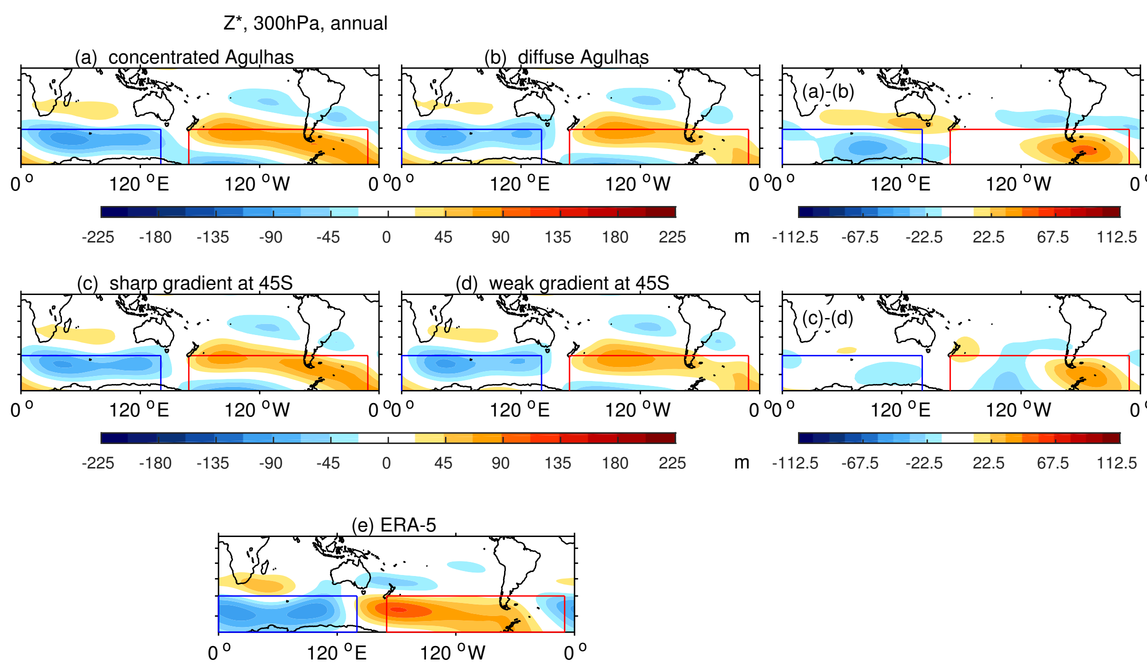

FIG. 14. As in Figure 11 but for the experiments probing the impact of the meridional surface temperature gradient near the Agulhas on the zonally asymmetric component of the geopotential height at 300hPa; (a)-(b) zonally confined perturbation; (c)-(d) zonally symmetric perturbation. (e) ERA-5 reanalysis (repeated from Figures 2a and 5a).

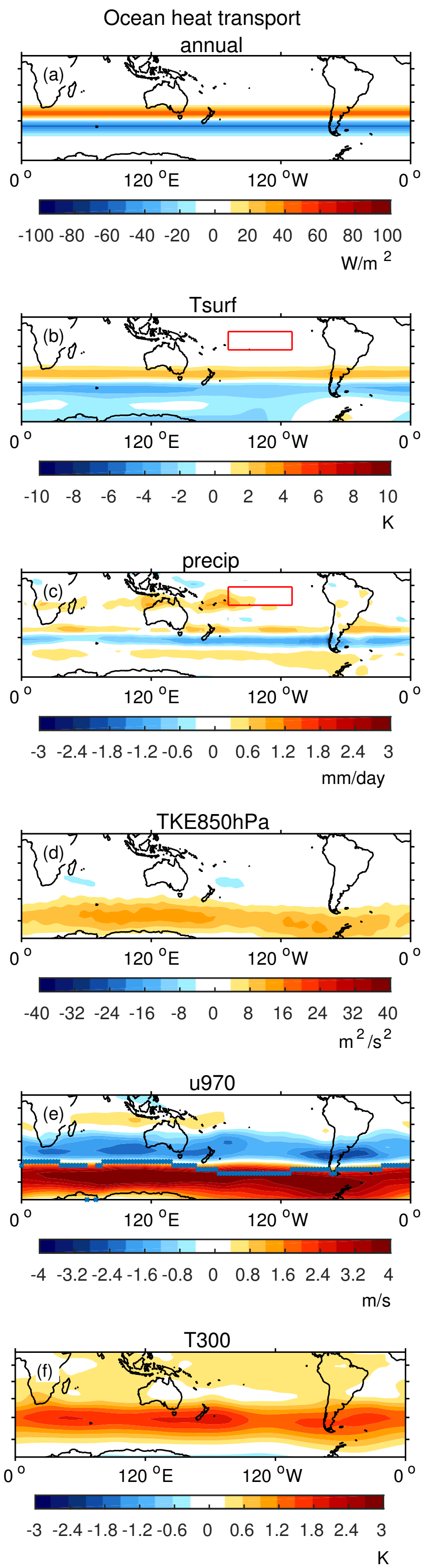

FIG. 15. As in the right column of Figure 13 but for a zonally symmetric ocean heat flux perturbation at the same latitudes of the perturbation imposed for Figure 13.